

Lepton flavor violating decays $l_j \rightarrow l_i \gamma$, $l_j \rightarrow 3l_i$ and $\mu \rightarrow e + q\bar{q}$ in the N-B-LSSM

Rong-Zhi Sun^{1,2,3}, Shu-Min Zhao^{1,2,3*}, Ming-Yue Liu^{1,2,3},

Xing-Yu Han^{1,2,3}, Song Gao^{1,2,3}, Xing-Xing Dong^{1,2,3,4†}

¹ *Department of Physics, Hebei University, Baoding 071002, China*

² *Hebei Key Laboratory of High-precision Computation and Application of Quantum Field Theory, Baoding, 071002, China*

³ *Hebei Research Center of the Basic Discipline for Computational Physics, Baoding, 071002, China and*

⁴ *Departamento de Fisica and CFTP, Instituto Superior Técnico, Universidade de Lisboa, Av.Rovisco Pais 1,1049-001 Lisboa, Portugal*

(Dated: February 26, 2025)

Abstract

The N-B-LSSM is an extension of the minimal supersymmetric standard model (MSSM) with the addition of three singlet new Higgs superfields and right-handed neutrinos, whose local gauge group is $SU(3)_C \times SU(2)_L \times U(1)_Y \times U(1)_{B-L}$. In the N-B-LSSM, we study lepton flavor violating decays $l_j \rightarrow l_i \gamma$, $l_j \rightarrow 3l_i$ and $\mu \rightarrow e + q\bar{q}$ ($j = \tau, \mu$, $i = \mu, e$ and $i \neq j$). Based on the current experimental limitations, we carry out detailed parameter scanning and numerical calculations to analyse the effects of different sensitive parameters on lepton flavor violation (LFV) in the N-B-LSSM. The numerical results show that the non-diagonal elements involving the initial and final leptons are main sensitive parameters and LFV sources. This work can provide a strong basis for exploring new physics (NP) beyond the Standard Model (SM).

PACS numbers:

Keywords: supersymmetry, lepton flavor violation, N-B-LSSM, new physics.

* zhaosm@hbu.edu.cn

† dongxx@hbu.edu.cn

I. INTRODUCTION

Over the past few decades, the successful observation of neutrino oscillations [1–3] has not only confirmed that neutrinos possess non-zero masses but also revealed significant lepton flavor mixing [4–7], thereby challenging the fundamental assumption of lepton flavor conservation in the SM. Although the SM has achieved remarkable success in describing strong, weak, and electromagnetic interactions, the presence of the Glashow-Iliopoulos-Maiani (GIM) mechanism leads to an extreme suppression of the predicted branching ratios for LFV decays [8]. For instance, the SM prediction for the branching ratio of $\mu \rightarrow e\gamma$ is as low as about 10^{-55} , far below the current experimental sensitivity. Consequently, any observation of LFV signals would provide compelling evidence for new physics (NP) beyond the SM. The paper summarizes the latest experimental results, including the upper limits on the LFV branching ratios of $l_j \rightarrow l_i\gamma$ and $l_j \rightarrow 3l_i$ at 90% confidence level (CL) [9], as well as the current sensitivities of $\mu - e$ conversion rates in different nuclei [10–12]:

$$\begin{aligned} \text{Br}(\mu \rightarrow e\gamma) &< 4.2 \times 10^{-13}, \quad \text{Br}(\mu \rightarrow 3e) < 1.0 \times 10^{-12}, \quad \text{CR}(\mu \rightarrow e : \text{Au}) < 7.0 \times 10^{-13}, \\ \text{Br}(\tau \rightarrow \mu\gamma) &< 4.2 \times 10^{-8}, \quad \text{Br}(\tau \rightarrow 3\mu) < 2.1 \times 10^{-8}, \quad \text{CR}(\mu \rightarrow e : \text{Ti}) < 4.3 \times 10^{-12}, \\ \text{Br}(\tau \rightarrow e\gamma) &< 3.3 \times 10^{-8}, \quad \text{Br}(\tau \rightarrow 3e) < 2.7 \times 10^{-8}, \quad \text{CR}(\mu \rightarrow e : \text{Pb}) < 4.6 \times 10^{-11}. \end{aligned} \quad (1)$$

To address the shortcomings of the SM in accounting for LFV phenomena, supersymmetry (SUSY) models have been widely investigated as extensions of the SM, with the MSSM being the most prominent example. However, the MSSM still has limitations in solving core challenges such as the μ problem [13] and the zero mass neutrino [14], which motivates the development of more comprehensive frameworks.

To further refine MSSM and overcome these issues, next to the minimal supersymmetric extension of the SM with local $B - L$ gauge symmetry (N-B-LSSM) has been proposed [15]. The key feature of this model is the incorporation of an additional $U(1)_{B-L}$ gauge symmetry, which extends the MSSM gauge group to $SU(3)_C \times SU(2)_L \times U(1)_Y \times U(1)_{B-L}$, where B denotes the baryon number and L represents the lepton number. This extension allows for a more natural explanation of neutrino masses and provides a framework for lepton and baryon number violation. One of the major innovations of N-B-LSSM is the introduction of right-handed neutrino superfields and three Higgs singlet superfields. This not only provides a natural mechanism for generating small neutrino masses through the seesaw mechanism but

also offers an effective solution to the μ problem, which MSSM fails to resolve. Specifically, in N-B-LSSM, the Higgs singlet \hat{S} , with a non-zero vacuum expectation value (VEV) of $\frac{v_S}{\sqrt{2}}$, couples to the up-type and down-type Higgs doublets H_u and H_d , generating the interaction term $\lambda \hat{S} \hat{H}_u \hat{H}_d$. This term replaces the traditional μ term in MSSM, resulting in an effective mass term $\lambda \frac{v_S}{\sqrt{2}} \hat{H}_u \hat{H}_d$, thus solving the μ problem without requiring additional fine-tuning. The extended Higgs sector leads to a 5×5 neutral CP-even Higgs mass matrix, which provides an explanation for the 125.20 ± 0.11 GeV Higgs mass. In the N-B-LSSM, the right-handed neutrinos, singlet Higgs fields, and the additional superfields effectively mitigate the little hierarchy problem in the MSSM through their higher VEVs. Assuming that the VEVs of these superfields are located at higher scales, the new particles' contributions to the model are effectively suppressed.

In supersymmetric extensions of the SM, both the $\mu\nu$ SSM [16, 17] and the ν_R MSSM [18] address the neutrino mass problem in the SM by introducing right-handed neutrinos (ν_R). On this basis, they also enhance the amplitudes of LFV decays. In the supersymmetric standard model with right-handed neutrino supermultiplets, the authors investigate various LFV processes in detail [19]. A minimal supersymmetric extension of the SM with local gauged B and L (BLMSSM) is first proposed by the author [20, 21]. The $\mu \rightarrow e$ conversion is investigated within the BLMSSM framework [22]. In Ref. [15], N-B-LSSM is proposed for the first time, which is the model adopted in this paper. In previous work, some two loop contribution to muon anomalous MDM in the N-B-LSSM is studied. This paper investigates the LFV processes ($\mu \rightarrow e\gamma$, $\tau \rightarrow e\gamma$, $\tau \rightarrow \mu\gamma$; $\mu \rightarrow 3e$, $\tau \rightarrow 3e$, $\tau \rightarrow 3\mu$; $\mu \rightarrow e + q\bar{q}$) in the framework of N-B-LSSM. We derive the corresponding Feynman diagrams, and the Feynman amplitudes, decay widths, branching ratios are analyzed numerically. Under the constraints of the latest experimental limits, sensitive and insensitive parameters are identified through one dimensional plots or scatter plots.

The structure of this paper is as follows. In Sec.II, we briefly summarize the main content of the N-B-LSSM. In Sec.III, we derive and present the analytical expressions for the branching ratios for $l_j \rightarrow l_i\gamma$ and $l_j \rightarrow 3l_i$, as well as the conversion rate for $\mu \rightarrow e + q\bar{q}$ within the N-B-LSSM framework. The input parameters and numerical analysis are detailed in Sec.IV. Our conclusions are presented in Sec.V. Finally, some mass matrices and couplings are collected in the Appendix A.

II. THE MAIN CONTENT OF N-B-LSSM

N-B-LSSM is an extension of MSSM, introducing an additional local gauge symmetry $U(1)_{B-L}$. The local gauge group of this model is $SU(3)_C \otimes SU(2)_L \otimes U(1)_Y \otimes U(1)_{B-L}$. Compared to MSSM, N-B-LSSM includes new superfields, such as right-handed neutrinos $\hat{\nu}_i$ and three Higgs singlets $\hat{\chi}_1$, $\hat{\chi}_2$, \hat{S} . The $U(1)_{B-L}$ symmetry is spontaneously broken by the VEVs of χ_1 and χ_2 , which also generate the large Majorana masses for right-handed neutrinos. Through the seesaw mechanism, light neutrinos obtain tiny masses at the tree level. The neutral CP-even parts of H_u , H_d , χ_1 , χ_2 and S mix with each other, forming a 5×5 mass squared matrix. The lightest mass eigenvalue within this matrix corresponds to the lightest CP-even Higgs. At the tree level, the theoretical Higgs mass generally does not match the experimentally observed value of 125.20 ± 0.11 GeV [23, 24]. To resolve this discrepancy, loop corrections must be included. As for sneutrinos, they are further classified into CP-even sneutrinos and CP-odd sneutrinos, and their mass squared matrices are expanded to 6×6 due to the inclusion of right-handed sneutrinos and their interactions.

The superpotential of N-B-LSSM is :

$$W = -Y_d \hat{d} \hat{q} \hat{H}_d - Y_e \hat{e} \hat{l} \hat{H}_d - \lambda_2 \hat{S} \hat{\chi}_1 \hat{\chi}_2 + \lambda \hat{S} \hat{H}_u \hat{H}_d + \frac{\kappa}{3} \hat{S} \hat{S} \hat{S} + Y_u \hat{u} \hat{q} \hat{H}_u + Y_\chi \hat{\nu} \hat{\chi}_1 \hat{\nu} + Y_\nu \hat{\nu} \hat{l} \hat{H}_u. \quad (2)$$

In the superpotential for this model, the Yukawa couplings are denoted by $Y_{u,d,e,\nu,\chi}$. While λ , λ_2 and κ represent dimensionless couplings. The fields $\hat{\chi}_1$, $\hat{\chi}_2$, \hat{S} are Higgs singlets. It is important to note that the term $Y'_\nu \hat{\nu} \hat{l} \hat{S}$ is not allowed, as the sum of $U(1)_Y$ charges of $\hat{\nu}$, \hat{l} , \hat{S} does not satisfy the necessary charge neutrality condition.

We show the concrete forms of the two Higgs doublets and three Higgs singlets

$$H_u = \begin{pmatrix} H_u^+ \\ \frac{1}{\sqrt{2}}(v_u + H_u^0 + iP_u^0) \end{pmatrix}, \quad H_d = \begin{pmatrix} \frac{1}{\sqrt{2}}(v_d + H_d^0 + iP_d^0) \\ H_d^- \end{pmatrix},$$

$$\chi_1 = \frac{1}{\sqrt{2}}(v_\eta + \phi_1^0 + iP_1^0), \quad \chi_2 = \frac{1}{\sqrt{2}}(v_{\bar{\eta}} + \phi_2^0 + iP_2^0), \quad S = \frac{1}{\sqrt{2}}(v_S + \phi_S^0 + iP_S^0). \quad (3)$$

The VEVs of the Higgs superfields H_u , H_d , χ_1 , χ_2 and S are presented by v_u , v_d , v_η , $v_{\bar{\eta}}$ and v_S respectively. Two angles are defined as $\tan \beta = v_u/v_d$ and $\tan \beta_\eta = v_{\bar{\eta}}/v_\eta$. The

definitions of $\tilde{\nu}_L$ and $\tilde{\nu}_R$ are:

$$\tilde{\nu}_L = \frac{1}{\sqrt{2}}\phi_L + \frac{i}{\sqrt{2}}\sigma_L, \quad \tilde{\nu}_R = \frac{1}{\sqrt{2}}\phi_R + \frac{i}{\sqrt{2}}\sigma_R. \quad (4)$$

The soft SUSY breaking terms of N-B-LSSM are shown as:

$$\begin{aligned} \mathcal{L}_{soft} = & \mathcal{L}_{soft}^{MSSM} - \frac{T_\kappa}{3}S^3 + \epsilon_{ij}T_\lambda SH_d^i H_u^j + T_2 S \chi_1 \chi_2 \\ & - T_{\chi,ik} \chi_1 \tilde{\nu}_{R,i}^* \tilde{\nu}_{R,k}^* + \epsilon_{ij} T_\nu H_u^i \tilde{\nu}_{R,i}^* \tilde{e}_{L,j} - m_\eta^2 |\chi_1|^2 - m_\eta^2 |\chi_2|^2 \\ & - m_S^2 |S|^2 - m_{\nu,ij}^2 \tilde{\nu}_{R,i}^* \tilde{\nu}_{R,j} - \frac{1}{2}(2M_{BB'} \lambda_{\tilde{B}} \tilde{B}' + M_{BL} \tilde{B}'^2) + h.c. \quad . \end{aligned} \quad (5)$$

In the Eq.(5), $\mathcal{L}_{soft}^{MSSM}$ represents the soft supersymmetry-breaking terms of MSSM. The parameters T_κ , T_λ , T_2 , T_χ and T_ν are trilinear coupling coefficients.

TABLE I: The superfields in N-B-LSSM

Superfields	$SU(3)_C$	$SU(2)_L$	$U(1)_Y$	$U(1)_{B-L}$
\hat{q}	3	2	1/6	1/6
\hat{l}	1	2	-1/2	-1/2
\hat{H}_d	1	2	-1/2	0
\hat{H}_u	1	2	1/2	0
\hat{d}	$\bar{3}$	1	1/3	-1/6
\hat{u}	$\bar{3}$	1	-2/3	-1/6
\hat{e}	1	1	1	1/2
$\hat{\nu}$	1	1	0	1/2
$\hat{\chi}_1$	1	1	0	-1
$\hat{\chi}_2$	1	1	0	1
\hat{S}	1	1	0	0

The particle content and charge distribution for N-B-LSSM are shown in the Table I. In the chiral superfields, $\hat{H}_u = (\hat{H}_u^+, \hat{H}_u^0)$ and $\hat{H}_d = (\hat{H}_d^0, \hat{H}_d^-)$ represent the MSSM-like Higgs doublet superfields. The superfields \hat{q} and \hat{l} are the doublets of quarks and leptons. The singlet superfields include \hat{u} , \hat{d} , \hat{e} and $\hat{\nu}$, which correspond to the up-type quark, down-type quark, charged lepton and neutrino superfields.

Y^Y signifies the $U(1)_Y$ charge, while Y^{B-L} denotes the $U(1)_{B-L}$ charge. The two Abelian groups, $U(1)_Y$ and $U(1)_{B-L}$, within the N-B-LSSM, produce a new effect: the gauge kinetic

mixing. This effect can be induced through RGEs, even when it starts from a zero value at M_{GUT} . Since both Abelian gauge groups remain unbroken, a basis transformation is permissible through the rotation matrix R ($R^T R = 1$) [25–28].

The form of the covariant derivatives of the N-B-LSSM can be written as:

$$D_\mu = \partial_\mu - i \begin{pmatrix} Y, & B - L \end{pmatrix} \begin{pmatrix} g_Y, & g'_{YB} \\ g'_{BY}, & g'_{B-L} \end{pmatrix} \begin{pmatrix} B_\mu^Y \\ B_\mu^{BL} \end{pmatrix}. \quad (6)$$

B_μ^Y and B_μ^{BL} denote the gauge fields pertaining to the $U(1)_Y$ and $U(1)_{B-L}$ respectively. Under the condition that the aforementioned Abelian gauge symmetry groups remain unbroken, the transformation of the basis is carried out through the application of a rotation matrix R .

$$D_\mu = \partial_\mu - i \begin{pmatrix} Y^Y, & Y^{B-L} \end{pmatrix} \begin{pmatrix} g_Y, & g'_{YB} \\ g'_{BY}, & g'_{B-L} \end{pmatrix} R^T R \begin{pmatrix} B_\mu^Y \\ B_\mu^{BL} \end{pmatrix}, \quad (7)$$

with the redefinitions

$$\begin{pmatrix} g_Y, & g'_{YB} \\ g'_{BY}, & g'_{B-L} \end{pmatrix} R^T = \begin{pmatrix} g_1, & g_{YB} \\ 0, & g_B \end{pmatrix} \quad \text{and} \quad R \begin{pmatrix} B_\mu^Y \\ B_\mu^{BL} \end{pmatrix} = \begin{pmatrix} B_\mu^Y \\ B_\mu^{BL} \end{pmatrix}, \quad (8)$$

Then the covariant derivatives of this model can be changed as

$$D_\mu = \partial_\mu - i \begin{pmatrix} Y^Y, & Y^{B-L} \end{pmatrix} \begin{pmatrix} g_1, & g_{YB} \\ 0, & g_B \end{pmatrix} \begin{pmatrix} B_\mu^Y \\ B_\mu^{BL} \end{pmatrix}. \quad (9)$$

Within the framework of this model, g_B is defined as the gauge coupling constant corresponding to the $U(1)_{B-L}$ group, and g_{YB} denotes the mixing gauge coupling constant of $U(1)_{B-L}$ group and $U(1)_Y$ group, the gauge bosons denoted by B_μ^Y , B_μ^{BL} and V_μ^3 intermingle at the tree level. The corresponding mass matrix is defined in the basis $(B_\mu^Y, B_\mu^{BL}, V_\mu^3)$:

$$\begin{pmatrix} \frac{1}{8}g_1^2v^2 & -\frac{1}{8}g_1g_2v^2 & \frac{1}{8}g_1(g_{YB} + g_B)v^2 \\ -\frac{1}{8}g_1g_2v^2 & \frac{1}{8}g_2^2v^2 & -\frac{1}{8}g_2(g_{YB} + g_B)v^2 \\ \frac{1}{8}g_1(g_{YB} + g_B)v^2 & -\frac{1}{8}g_2(g_{YB} + g_B)v^2 & \frac{1}{8}(g_{YB} + g_B)^2v^2 + \frac{1}{8}g_B^2\xi^2 \end{pmatrix}, \quad (10)$$

with $v^2 = v_u^2 + v_d^2$ and $\xi^2 = v_\eta^2 + v_\eta^2$. The mass matrix in Eq.(10) is diagonalized using the Weinberg angle θ_W and the new mixing angles θ'_W . θ'_W is defined from the following formula:

$$\sin^2 \theta'_W = \frac{1}{2} - \frac{[(g_{YB} + g_B)^2 - g_1^2 - g_2^2]v^2 + 4g_B^2\xi^2}{2\sqrt{[(g_{YB} + g_B)^2 + g_1^2 + g_2^2]^2v^4 + 8g_B^2[(g_{YB} + g_B)^2 - g_1^2 - g_2^2]v^2\xi^2 + 16g_B^4\xi^4}}. \quad (11)$$

We deduce the eigenvalues of Eq.(10)

$$\begin{aligned} m_\gamma^2 &= 0, \\ m_{Z,Z'}^2 &= \frac{1}{8} \left([g_1^2 + g_2^2 + (g_{YB} + g_B)^2]v^2 + 4g_B^2\xi^2 \right. \\ &\quad \left. \mp \sqrt{[g_1^2 + g_2^2 + (g_{YB} + g_B)^2]^2v^4 + 8[(g_{YB} + g_B)^2 - g_1^2 - g_2^2]g_B^2v^2\xi^2 + 16g_B^4\xi^4} \right). \end{aligned} \quad (12)$$

We show some used mass matrixes and couplings in the Appendix A.

III. FORMULATION

In this section, the LFV processes $l_j \rightarrow l_i\gamma$, $l_j \rightarrow 3l_i$ ($j = \tau, \mu$, $i = \mu, e$ and $i \neq j$) and $\mu \rightarrow e + q\bar{q}$ are studied in the N-B-LSSM. The effective Lagrangian is affected by contributions from one-loop, triangle-type, penguin-type, self-energy and box-type diagrams. For convenience, these diagrams are analyzed in the generic form, which can simplify the work.

A. $l_j \rightarrow l_i\gamma$

The relevant Feynman diagrams are shown in Fig.1. When the external leptons are all on shell, the amplitudes for $l_j \rightarrow l_i\gamma$ can be expressed in the following general form:

$$\begin{aligned} \mathcal{M} &= e\epsilon^\mu \bar{u}_i(p+q) \left[q^2 \gamma_\mu (A_1^L P_L + A_1^R P_R) \right. \\ &\quad \left. + m_{l_j} i\sigma_{\mu\nu} q^\nu (A_2^L P_L + A_2^R P_R) \right] u_j(p), \end{aligned} \quad (13)$$

where p denotes the injecting lepton momentum, q represents the photon momentum, and m_{l_j} is the mass of the charged lepton in the j th generation. The wave function for the external leptons are given by $u_i(p)$ and $v_i(p)$. The final Wilson coefficients $A_1^L, A_1^R, A_2^L, A_2^R$ are determined by summing the amplitudes of the corresponding diagrams.

The contributions from the virtual neutral fermion diagrams are denoted by $A_\alpha^{L,R}(n)$, $\alpha = 1, 2$. The derived results are presented in the following form:

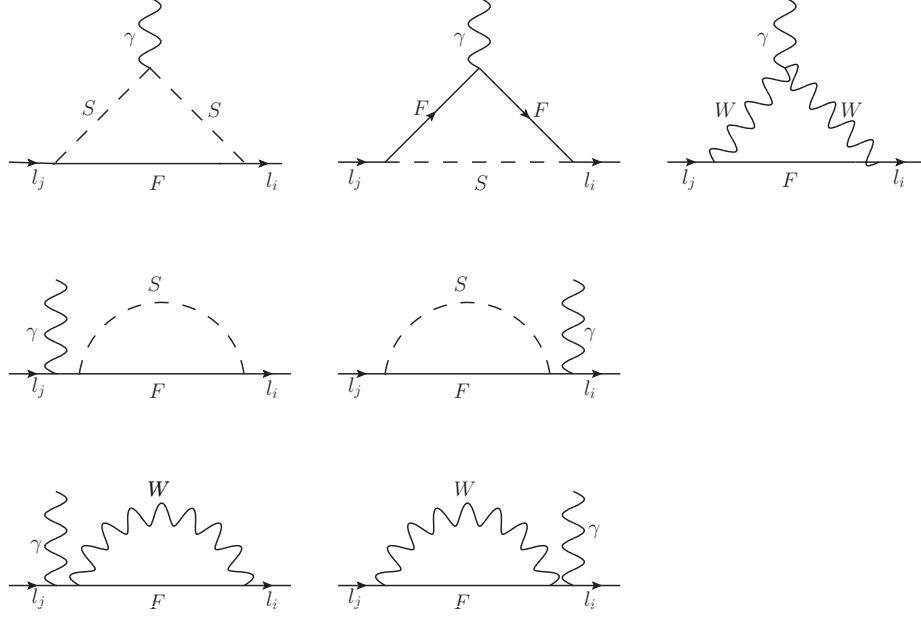


FIG. 1: The one-loop diagrams for $l_j \rightarrow l_i \gamma$, with F representing Dirac (Majorana) particles.

$$\begin{aligned}
A_1^L(n) &= \sum_{\beta=1}^8 \sum_{\alpha=1}^6 \frac{1}{6m_W^2} C_R^{\tilde{L}_\alpha \chi_\beta^0 \bar{l}_i} C_L^{\tilde{L}_\alpha^* l_j \bar{\chi}_\beta^0} F_1(x_{\chi_\beta^0}, x_{\tilde{L}_\alpha}) \\
&\quad + \sum_{\delta=1}^6 \sum_{\vartheta=1}^2 \frac{1}{6m_W^2} C_R^{H_\vartheta^\pm \nu_\delta \bar{l}_i} C_L^{H_\vartheta^{\pm*} l_j \bar{\nu}_\delta} F_1(x_{\nu_\delta}, x_{H_\vartheta^\pm}), \\
A_2^L(n) &= \sum_{\beta=1}^8 \sum_{\alpha=1}^6 \frac{m_{\chi_\beta^0}}{m_{l_j} m_W^2} C_L^{\tilde{L}_\alpha \chi_\beta^0 \bar{l}_i} C_L^{\tilde{L}_\alpha^* l_j \bar{\chi}_\beta^0} F_2(x_{\chi_\beta^0}, x_{\tilde{L}_\alpha}) \\
&\quad + \sum_{\delta=1}^6 \sum_{\vartheta=1}^2 \frac{m_{\nu_\delta}}{m_{l_j} m_W^2} C_L^{H_\vartheta^\pm \nu_\delta \bar{l}_i} C_L^{H_\vartheta^{\pm*} l_j \bar{\nu}_\delta} F_2(x_{\nu_\delta}, x_{H_\vartheta^\pm}), \\
A_\alpha^R(n) &= A_\alpha^L(n) \Big|_{L \leftrightarrow R}, \quad \alpha = 1, 2.
\end{aligned} \tag{14}$$

Here, $x_i = m_i^2/m_W^2$ with m_i denoting the mass of the corresponding particle, the one-loop functions $F_1(x, y)$ and $F_2(x, y)$ are compiled as follows:

$$\begin{aligned}
F_1(x, y) &= \frac{1}{96\pi^2} \left[\frac{7xy - 11x^2 - 2y^2}{(x-y)^3} + \frac{6x^3(\ln x - \ln y)}{(x-y)^4} \right], \\
F_2(x, y) &= \frac{1}{32\pi^2} \left[-\frac{x+y}{(x-y)^2} + \frac{2xy(\ln x - \ln y)}{(x-y)^3} \right].
\end{aligned} \tag{15}$$

The coefficients $A_\alpha^{L,R}(c)$, $\alpha = 1, 2$ represent contributions from the virtual charged fermion

diagrams and the expressions are:

$$\begin{aligned}
A_1^L(c) &= \sum_{\rho=1}^2 \sum_{\sigma=1}^6 \frac{1}{6m_W^2} C_R^{\tilde{\nu}_\sigma \chi_\rho^\pm \bar{l}_i} C_L^{\tilde{\nu}_\sigma^* l_j \bar{\chi}_\rho^\pm} F_3(x_{\chi_\rho^\pm}, x_{\tilde{\nu}_\sigma}), \\
A_2^L(c) &= \sum_{\rho=1}^2 \sum_{\sigma=1}^6 \frac{m_{\chi_\rho^\pm}}{m_{l_j} m_W^2} C_L^{\tilde{\nu}_\sigma \chi_\rho^\pm \bar{l}_i} C_L^{\tilde{\nu}_\sigma^* l_j \bar{\chi}_\rho^\pm} F_4(x_{\chi_\rho^\pm}, x_{\tilde{\nu}_\sigma}), \\
A_\alpha^R(c) &= A_\alpha^L(c)|_{L \leftrightarrow R}, \quad \alpha = 1, 2.
\end{aligned} \tag{16}$$

with

$$\begin{aligned}
F_3(x, y) &= \frac{1}{96\pi^2} \left[\frac{29xy - 7x^2 - 16y^2}{(x-y)^3} - \frac{6y^2(3x-2y)(\ln x - \ln y)}{(x-y)^4} \right], \\
F_4(x, y) &= \frac{1}{96\pi^2} \left[-\frac{-17xy + x^2 + 10y^2}{(x-y)^3} - \frac{6y(x^2 + xy - y^2)(\ln x - \ln y)}{(x-y)^4} \right].
\end{aligned} \tag{17}$$

In this paper, $\tilde{\nu}$ encompasses both $\tilde{\nu}^R$ and $\tilde{\nu}^I$.

The mixing of three light neutrinos with three heavy neutrinos introduces corrections to the LFV processes $l_j \rightarrow l_i \gamma$ through virtual W diagrams. The corresponding coefficients are denoted as $A_\alpha^{L,R}(W)$, $\alpha = 1, 2$.

$$\begin{aligned}
A_1^L(W) &= \sum_{\delta=1}^6 \frac{-1}{2m_W^2} C_L^{W \nu_\delta \bar{l}_i} C_L^{W^* l_j \bar{\nu}_\delta} F_5(x_{\nu_\delta}, x_W), \\
A_2^L(W) &= \sum_{\delta=1}^6 \frac{1}{m_W^2} C_L^{W \nu_\delta \bar{l}_i} C_L^{W^* l_j \bar{\nu}_\delta} \left(1 + \frac{m_{l_i}}{m_{l_j}}\right) F_6(x_{\nu_\delta}, x_W), \\
A_\alpha^R(W) &= 0, \quad \alpha = 1, 2.
\end{aligned} \tag{18}$$

with

$$\begin{aligned}
F_5(x, y) &= \frac{1}{96\pi^2} \left[\frac{19xy - 20x^2 - 5y^2}{(x-y)^3} + \frac{6x^2(2x-y)(\ln x - \ln y)}{(x-y)^4} \right], \\
F_6(x, y) &= \frac{1}{288\pi^2} \left[\frac{65xy - 43x^2 - 16y^2}{(x-y)^3} + \frac{6x^2(5x-6y)(\ln x - \ln y)}{(x-y)^4} \right].
\end{aligned} \tag{19}$$

The final Wilson coefficients are obtained by summing the expressions in Eqs.(14)(16)(18) and the decay width for $l_j \rightarrow l_i \gamma$ can be expressed by Eq.(13):

$$\begin{aligned}
A_\alpha^{L,R} &= A_\alpha^{L,R}(n) + A_\alpha^{L,R}(c) + A_\alpha^{L,R}(W), \quad \alpha = 1, 2, \\
\Gamma(l_j \rightarrow l_i \gamma) &= \frac{e^2}{16\pi} m_{l_j}^5 (|A_2^L|^2 + |A_2^R|^2).
\end{aligned} \tag{20}$$

Finally, we get the branching ratio of $l_j \rightarrow l_i \gamma$:

$$Br(l_j \rightarrow l_i \gamma) = \frac{\Gamma(l_j \rightarrow l_i \gamma)}{\Gamma_{l_j}}. \tag{21}$$

B. $l_j \rightarrow 3l_i$

The effective Lagrangian for $l_j \rightarrow 3l_i$ decay processes receive contributions from penguin-type (γ -penguin and Z -penguin), self-energy diagrams and box-type diagrams. Let's first analyze the impact of the penguin-type and self-energy diagrams illustrated in Fig.2. on this transition mechanism.

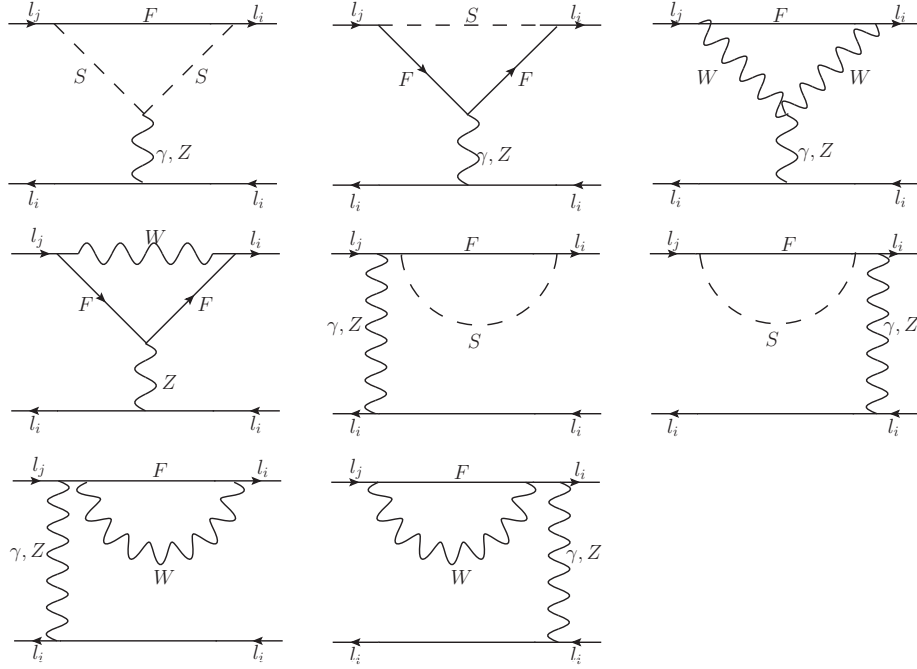


FIG. 2: The penguin-type and self-energy diagrams for $l_j \rightarrow 3l_i$, with F representing Dirac (Majorana) particles.

Using Eq.(13), the contributions from the γ -penguin can be derived and expressed in the following form:

$$T_{\gamma-p} = \bar{u}_i(p_1)[q^2\gamma_\mu(A_1^L P_L + A_1^R P_R) + m_{l_j}i\sigma_{\mu\nu}q^\nu(A_2^L P_L + A_2^R P_R)]u_j(p) \\ \times \frac{e^2}{q^2}\bar{u}_i(p_2)\gamma^\mu v_i(p_3) - (p_1 \leftrightarrow p_2). \quad (22)$$

The contributions from Z -penguin diagrams are derived following the same procedure as that used for the γ -penguin diagrams.

$$T_{Z-p} = \frac{e^2}{m_Z^2}\bar{u}_i(p_1)\gamma_\mu(D_L P_L + D_R P_R)u_j(p)\bar{u}_i(p_2)\gamma^\mu(C_L^{Zl_i\bar{l}_i} P_L + C_R^{Zl_i\bar{l}_i} P_R)v_i(p_3) \\ - (p_1 \leftrightarrow p_2). \\ D_{L,R} = D_{L,R}(S) + D_{L,R}(W). \quad (23)$$

The explicit expressions for the effective couplings are given by

$$\begin{aligned}
D_L(S) = & \frac{1}{2e^2} \left\{ \left[\sum_{\alpha=1}^6 \sum_{\beta,n=1}^8 \left(\frac{2m_{\chi_\beta^0} m_{\chi_n^0}}{m_W^2} C_R^{\tilde{L}_\alpha \chi_n^0 \bar{l}_i} C_L^{Z \chi_\beta^0 \bar{\chi}_n^0} C_L^{\tilde{L}_\alpha^* l_j \bar{\chi}_\beta^0} E_1(x_{\tilde{L}_\alpha}, x_{\chi_n^0}, x_{\chi_\beta^0}) \right. \right. \right. \\
& - C_R^{\tilde{L}_\alpha \chi_n^0 \bar{l}_i} C_R^{Z \chi_\beta^0 \bar{\chi}_n^0} C_L^{\tilde{L}_\alpha^* l_j \bar{\chi}_\beta^0} E_2(x_{\tilde{L}_\alpha}, x_{\chi_n^0}, x_{\chi_\beta^0}) \Big) \\
& + \sum_{\kappa=1}^8 \sum_{\rho,\sigma=1}^6 C_R^{\tilde{L}_\sigma \chi_\kappa^0 \bar{l}_i} C^{Z \tilde{L}_\rho \tilde{L}_\sigma^*} C_L^{\tilde{L}_\rho^* l_j \bar{\chi}_\kappa^0} E_2(x_{\chi_\kappa^0}, x_{\tilde{L}_\rho}, x_{\tilde{L}_\sigma}) \Big] \\
& + \left[\sum_{\zeta=1}^6 \sum_{\eta,\theta=1}^2 \left(\frac{2m_{\chi_\eta^\pm} m_{\chi_\theta^\pm}}{m_W^2} C_R^{\tilde{\nu}_\zeta \chi_\eta^\pm \bar{l}_i} C_L^{Z \chi_\eta^\pm \bar{\chi}_\theta^\pm} C_L^{\tilde{\nu}_\zeta^* l_j \bar{\chi}_\eta^\pm} E_1(x_{\tilde{\nu}_\zeta}, x_{\chi_\theta^\pm}, x_{\chi_\eta^\pm}) \right. \right. \\
& - C_R^{\tilde{\nu}_\zeta \chi_\theta^\pm \bar{l}_i} C_R^{Z \chi_\eta^\pm \bar{\chi}_\theta^\pm} C_L^{\tilde{\nu}_\zeta^* l_j \bar{\chi}_\eta^\pm} E_2(x_{\tilde{\nu}_\zeta}, x_{\chi_\theta^\pm}, x_{\chi_\eta^\pm}) \Big) \\
& + \sum_{\xi=1}^2 \sum_{\iota,\epsilon=1}^6 C_R^{\tilde{\nu}_\epsilon \chi_\xi^\pm \bar{l}_i} C^{Z \tilde{\nu}_\iota \tilde{\nu}_\epsilon^*} C_L^{\tilde{\nu}_\iota^* l_j \bar{\chi}_\xi^\pm} E_2(x_{\chi_\xi^\pm}, x_{\tilde{\nu}_\iota}, x_{\tilde{\nu}_\epsilon}) \Big] \\
& + \left[\sum_{\vartheta=1}^2 \sum_{\delta,\varpi=1}^6 \left(\frac{2m_{\nu_\delta} m_{\nu_\varpi}}{m_W^2} C_R^{H_\vartheta^\pm \nu_\varpi \bar{l}_i} C_L^{Z \nu_\delta \bar{\nu}_\varpi} C_L^{H_\vartheta^{\pm*} l_j \bar{\nu}_\delta} E_1(x_{H_\vartheta^\pm}, x_{\nu_\varpi}, x_{\nu_\delta}) \right. \right. \\
& - C_R^{H_\vartheta^\pm \nu_\varpi \bar{l}_i} C_L^{Z \nu_\delta \bar{\nu}_\varpi} C_L^{H_\vartheta^{\pm*} l_j \bar{\nu}_\delta} E_2(x_{H_\vartheta^\pm}, x_{\nu_\varpi}, x_{\nu_\delta}) \Big) \\
& + \sum_{\varrho=1}^6 \sum_{\phi,\varphi=1}^2 C_R^{H_\varphi^\pm \nu_\varrho \bar{l}_i} C^{Z H_\phi^\pm H_\varphi^{\pm*}} C_L^{H_\phi^{\pm*} l_j \bar{\nu}_\varrho} E_2(x_{\nu_\varrho}, x_{H_\phi^\pm}, x_{H_\varphi^\pm}) \Big] \Big\}, \\
D_R(S) = & D_L(S)|_{L \leftrightarrow R}.
\end{aligned} \tag{24}$$

The functions $E_1(x, y, z)$ and $E_2(x, y, z)$ are defined as follows:

$$\begin{aligned}
E_1(x, y, z) = & \frac{1}{16\pi^2} \left[\frac{x \ln x}{(x-y)(x-z)} + \frac{y \ln y}{(y-x)(y-z)} + \frac{z \ln z}{(z-x)(z-y)} \right], \\
E_2(x, y, z) = & \frac{1}{16\pi^2} \left[-(\Delta + 1 + \ln x_\mu) + \frac{x^2 \ln x}{(x-y)(x-z)} \right. \\
& \left. + \frac{y^2 \ln y}{(y-x)(y-z)} + \frac{z^2 \ln z}{(z-x)(z-y)} \right].
\end{aligned} \tag{25}$$

We keep the small m_i term and calculate the specific form of $D_{L,R}(W)$,

$$\begin{aligned}
D_L(W) = & \frac{c_W}{e s_W} \sum_{\delta=1}^6 C_L^{W \nu_\delta \bar{l}_i} C_L^{W^* l_j \bar{\nu}_\delta} \left[E_3(x_{\nu_\delta}, x_W) + 2(x_i + x_j) E_6(x_{\nu_\delta}, x_W) \right] \\
& + \frac{1}{e^2} \sum_{\varpi,\varrho=1}^6 C_L^{W \nu_\varrho \bar{l}_i} C_L^{W^* l_j \bar{\nu}_\varpi} C_L^{Z^* \nu_\varpi \bar{\nu}_\varrho} \left\{ -\frac{3}{32\pi^2} - E_2(x_W, x_{\nu_\varpi}, x_{\nu_\varrho}) \right. \\
& \left. + x_j \left[\frac{1}{3} E_4(x_W, x_{\nu_\varpi}, x_{\nu_\varrho}) + E_5(x_W, x_{\nu_\varpi}, x_{\nu_\varrho}) \right] \right\},
\end{aligned}$$

$$\begin{aligned}
D_R(W) = & \frac{c_W}{e s_W} \sum_{\delta=1}^6 C_L^{W\nu_\delta \bar{l}_i} C_L^{W* l_j \bar{\nu}_\delta} 2\sqrt{x_i x_j} E_6(x_{\nu_\delta}, x_W) \\
& + \frac{1}{e^2} \sum_{\varpi, \varrho=1}^6 C_L^{W\nu_\varrho \bar{l}_i} C_L^{W* l_j \bar{\nu}_\varpi} C_L^{Z* \nu_\varpi \bar{\nu}_\varrho} \sqrt{x_i x_j} \left[2E_1(x_W, x_{\nu_\varpi}, x_{\nu_\varrho}) \right. \\
& \left. - \frac{1}{3} E_4(x_W, x_{\nu_\varpi}, x_{\nu_\varrho}) - 2E_5(x_W, x_{\nu_\varpi}, x_{\nu_\varrho}) \right]. \tag{26}
\end{aligned}$$

Here, $x_i = m_{l_i}^2/m_W^2$ and $x_j = m_{l_j}^2/m_W^2$.

The concrete expressions for the functions $E_3(x, y)$, $E_4(x, y, z)$, $E_5(x, y, z)$ and $E_6(x, y)$ are collected here

$$\begin{aligned}
E_3(x, y) &= \frac{-1}{16\pi^2} \left[(\Delta + \ln x_\mu + 1) + \frac{y^2 \ln y - x^2 \ln x}{(y-x)^2} + \frac{y + 2y \ln y}{x-y} - \frac{1}{2} \right], \\
E_4(x, y, z) &= \frac{1}{32\pi^2} \left[\frac{2x^3[3x(x-y-z) + y^2 + yz + z^2] \ln x}{(x-y)^3(x-z)^3} \right. \\
&\quad - \frac{2(3x^2 - 3xy + y^2)y \ln y}{(x-y)^3(y-z)} + \frac{2(3x^2 - 3xz + z^2)z \ln z}{(x-z)^3(y-z)} \\
&\quad \left. - \frac{x[5x^2 - 3x(y+z) + yz]}{(x-y)^2(x-z)^2} \right], \\
E_5(x, y, z) &= \frac{1}{16\pi^2} \left[\frac{x^2(2x-y-z) \ln x}{(x-y)^2(x-z)^2} + \frac{y(y-2x) \ln y}{(x-y)^2(y-z)} \right. \\
&\quad \left. - \frac{x}{(x-y)(x-z)} + \frac{z(2x-z) \ln z}{(x-z)^2(y-z)} \right], \\
E_6(x, y) &= \frac{1}{96\pi^2} \left[\frac{6x^2 y (\ln x - \ln y)}{(x-y)^4} + \frac{-5xy - 2x^2 + y^2}{(x-y)^3} \right]. \tag{27}
\end{aligned}$$

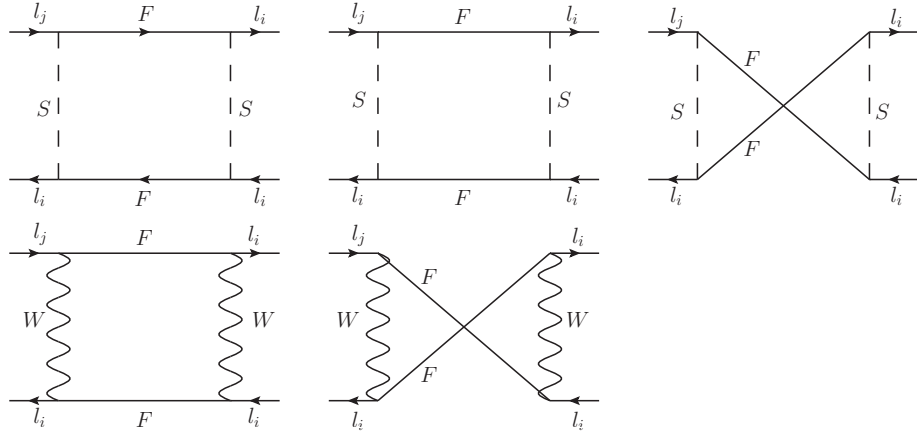


FIG. 3: The box-type diagrams for $l_j \rightarrow 3l_i$, with F representing Dirac (Majorana) particles.

The box-type diagrams depicted in Fig.3 can be expressed in the following form:

$$\begin{aligned}
T_{box} = & \left\{ B_1^L e^2 \bar{u}_i(p_1) \gamma_\mu P_L u_j(p) \bar{u}_i(p_2) \gamma^\mu P_L v_i(p_3) + (L \leftrightarrow R) \right\} \\
& + \left\{ B_2^L e^2 \left[\bar{u}_i(p_1) \gamma_\mu P_L u_j(p) \bar{u}_i(p_2) \gamma^\mu P_R v_i(p_3) - (p_1 \leftrightarrow p_2) \right] + (L \leftrightarrow R) \right\} \\
& + \left\{ B_3^L e^2 \left[\bar{u}_i(p_1) P_L u_j(p) \bar{u}_i(p_2) P_L v_i(p_3) - (p_1 \leftrightarrow p_2) \right] + (L \leftrightarrow R) \right\} \\
& + \left\{ B_4^L e^2 \left[\bar{u}_i(p_1) \sigma_{\mu\nu} P_L u_j(p) \bar{u}_i(p_2) \sigma^{\mu\nu} P_L v_i(p_3) - (p_1 \leftrightarrow p_2) \right] + (L \leftrightarrow R) \right\} \\
& + \left\{ B_5^L e^2 \left[\bar{u}_i(p_1) P_L u_j(p) \bar{u}_i(p_2) P_R v_i(p_3) - (p_1 \leftrightarrow p_2) \right] + (L \leftrightarrow R) \right\}. \tag{28}
\end{aligned}$$

The virtual chargino contributions to the effective couplings $B_\beta^{L,R}(c)$, $\beta = 1...5$ are determined from the box-type diagrams.

$$\begin{aligned}
B_1^L(c) &= \sum_{\eta, \theta=1}^2 \sum_{\epsilon, \iota=1}^6 \frac{1}{2e^2 m_W^2} C_R^{\tilde{\nu}_\iota \chi_\eta^\pm \bar{l}_i} C_L^{\tilde{\nu}_\epsilon l_j \bar{\chi}_\eta^\pm} C_R^{\tilde{\nu}_\epsilon \chi_\theta^\pm \bar{l}_i} C_L^{\tilde{\nu}_\iota l_i \bar{\chi}_\theta^\pm} E_7(x_{\chi_\eta^\pm}, x_{\chi_\theta^\pm}, x_{\tilde{\nu}_\epsilon}, x_{\tilde{\nu}_\iota}), \\
B_2^L(c) &= \sum_{\eta, \theta=1}^2 \sum_{\epsilon, \iota=1}^6 \left[\frac{1}{4e^2 m_W^2} C_R^{\tilde{\nu}_\iota \chi_\eta^\pm \bar{l}_i} C_L^{\tilde{\nu}_\epsilon l_j \bar{\chi}_\eta^\pm} C_L^{\tilde{\nu}_\epsilon \chi_\theta^\pm \bar{l}_i} C_R^{\tilde{\nu}_\iota l_i \bar{\chi}_\theta^\pm} E_7(x_{\chi_\eta^\pm}, x_{\chi_\theta^\pm}, x_{\tilde{\nu}_\epsilon}, x_{\tilde{\nu}_\iota}), \right. \\
&\quad \left. - \frac{m_{\chi_\eta^\pm} m_{\chi_\theta^\pm}}{2e^2 m_W^4} C_R^{\tilde{\nu}_\iota \chi_\eta^\pm \bar{l}_i} C_L^{\tilde{\nu}_\epsilon l_j \bar{\chi}_\eta^\pm} C_L^{\tilde{\nu}_\epsilon \chi_\theta^\pm \bar{l}_i} C_L^{\tilde{\nu}_\iota l_i \bar{\chi}_\theta^\pm} E_8(x_{\chi_\eta^\pm}, x_{\chi_\theta^\pm}, x_{\tilde{\nu}_\epsilon}, x_{\tilde{\nu}_\iota}) \right], \\
B_3^L(c) &= \sum_{\eta, \theta=1}^2 \sum_{\epsilon, \iota=1}^6 \frac{m_{\chi_\eta^\pm} m_{\chi_\theta^\pm}}{e^2 m_W^4} C_L^{\tilde{\nu}_\iota \chi_\eta^\pm \bar{l}_i} C_L^{\tilde{\nu}_\epsilon l_j \bar{\chi}_\eta^\pm} C_L^{\tilde{\nu}_\epsilon \chi_\theta^\pm \bar{l}_i} C_L^{\tilde{\nu}_\iota l_i \bar{\chi}_\theta^\pm} E_8(x_{\chi_\eta^\pm}, x_{\chi_\theta^\pm}, x_{\tilde{\nu}_\epsilon}, x_{\tilde{\nu}_\iota}), \\
B_4^L(c) &= B_5^L(c) = 0, \\
B_\beta^R(c) &= B_\beta^L(c)|_{L \leftrightarrow R}, \quad \beta = 1...5, \tag{29}
\end{aligned}$$

with

$$\begin{aligned}
E_7(x, y, z, t) &= \frac{1}{16\pi^2} \left[\frac{x^2 \ln x}{(x-y)(x-z)(x-t)} + \frac{y^2 \ln y}{(y-x)(y-z)(y-t)} \right. \\
&\quad \left. + \frac{z^2 \ln z}{(z-x)(z-y)(z-t)} + \frac{t^2 \ln t}{(t-x)(t-y)(t-z)} \right], \\
E_8(x, y, z, t) &= \frac{1}{16\pi^2} \left[\frac{x \ln x}{(x-y)(x-z)(x-t)} + \frac{y \ln y}{(y-x)(y-z)(y-t)} \right. \\
&\quad \left. + \frac{z \ln z}{(z-x)(z-y)(z-t)} + \frac{t \ln t}{(t-x)(t-y)(t-z)} \right]. \tag{30}
\end{aligned}$$

For the box-type diagrams, the neutralino-slepton, neutrino-charged Higgs and lepton neutralino-slepton contributions to the effective couplings $B_\beta^{L,R}(n)$, $\beta = 1...5$ are written,

$$B_1^L(n) = \sum_{\beta, n=1}^8 \sum_{\rho, \sigma=1}^6 \left\{ \frac{m_{\chi_\beta^0} m_{\chi_n^0}}{e^2 m_W^4} E_8(x_{\chi_\beta^0}, x_{\chi_n^0}, x_{\tilde{L}_\rho}, x_{\tilde{L}_\sigma}) C_L^{\tilde{L}_\sigma \chi_\beta^0 \bar{l}_i} C_L^{\tilde{L}_\rho^* l_j \bar{\chi}_\beta^0} C_R^{\tilde{L}_\sigma \chi_n^0 \bar{l}_i} C_R^{\tilde{L}_\rho^* l_i \bar{\chi}_n^0} \right\}$$

$$\begin{aligned}
& + \frac{1}{2e^2 m_W^2} E_7(x_{\chi_\beta^0}, x_{\chi_n^0}, x_{\tilde{L}_\rho}, x_{\tilde{L}_\sigma}) \left[C_R^{\tilde{L}_\sigma \chi_\beta^0 \bar{l}_i} C_L^{\tilde{L}_\rho^* l_j \bar{\chi}_\beta^0} C_R^{\tilde{L}_\rho \chi_n^0 \bar{l}_i} C_L^{\tilde{L}_\sigma^* l_i \bar{\chi}_n^0} \right. \\
& + \left. C_L^{\tilde{L}_\sigma \chi_\beta^0 \bar{l}_i} C_R^{\tilde{L}_\rho^* l_j \bar{\chi}_\beta^0} C_R^{\tilde{L}_\sigma \chi_n^0 \bar{l}_i} C_L^{\tilde{L}_\rho^* l_i \bar{\chi}_n^0} \right] \\
& + \sum_{\varpi, \varrho=1}^6 \sum_{\phi, \varphi=1}^2 \left\{ \frac{m_{\nu_\varpi} m_{\nu_\varrho}}{e^2 m_W^4} E_8(x_{\nu_\varpi}, x_{\nu_\varrho}, x_{H_\phi^\pm}, x_{H_\varphi^\pm}) C_L^{H_\varphi^\pm \nu_\varpi \bar{l}_i} C_L^{H_\phi^\pm^* l_j \bar{\nu}_\varpi} C_R^{H_\varphi^\pm \nu_\varrho \bar{l}_i} C_R^{H_\phi^\pm^* l_i \bar{\nu}_\varrho} \right. \\
& + \frac{1}{2e^2 m_W^2} E_7(x_{\nu_\varpi}, x_{\nu_\varrho}, x_{H_\phi^\pm}, x_{H_\varphi^\pm}) \left[C_R^{H_\varphi^\pm \nu_\varpi \bar{l}_i} C_L^{H_\phi^\pm^* l_j \bar{\nu}_\varpi} C_R^{H_\phi^\pm \nu_\varrho \bar{l}_i} C_L^{H_\varphi^\pm^* l_i \bar{\nu}_\varrho} \right. \\
& + \left. C_L^{H_\varphi^\pm \nu_\varpi \bar{l}_i} C_R^{H_\phi^\pm^* l_j \bar{\nu}_\varpi} C_R^{H_\varphi^\pm \nu_\varrho \bar{l}_i} C_L^{H_\phi^\pm^* l_i \bar{\nu}_\varrho} \right] \left. \right\}, \\
B_2^L(n) = & \sum_{\beta, n=1}^8 \sum_{\rho, \sigma=1}^6 \left\{ -\frac{m_{\chi_\beta^0} m_{\chi_n^0}}{2e^2 m_W^4} E_8(x_{\chi_\beta^0}, x_{\chi_n^0}, x_{\tilde{L}_\rho}, x_{\tilde{L}_\sigma}) C_R^{\tilde{L}_\sigma \chi_\beta^0 \bar{l}_i} C_R^{\tilde{L}_\rho^* l_j \bar{\chi}_\beta^0} C_L^{\tilde{L}_\rho \chi_n^0 \bar{l}_i} C_L^{\tilde{L}_\sigma^* l_i \bar{\chi}_n^0} \right. \\
& + \frac{1}{4e^2 m_W^2} E_7(x_{\chi_\beta^0}, x_{\chi_n^0}, x_{\tilde{L}_\rho}, x_{\tilde{L}_\sigma}) \left[C_R^{\tilde{L}_\sigma \chi_\beta^0 \bar{l}_i} C_L^{\tilde{L}_\rho^* l_j \bar{\chi}_\beta^0} C_L^{\tilde{L}_\rho \chi_n^0 \bar{l}_i} C_R^{\tilde{L}_\sigma^* l_i \bar{\chi}_n^0} \right. \\
& + \left. C_R^{\tilde{L}_\sigma \chi_\beta^0 \bar{l}_i} C_L^{\tilde{L}_\rho^* l_j \bar{\chi}_\beta^0} C_R^{\tilde{L}_\sigma \chi_n^0 \bar{l}_i} C_L^{\tilde{L}_\rho^* l_i \bar{\chi}_n^0} \right] \left. \right\} \\
& + \sum_{\varpi, \varrho=1}^6 \sum_{\phi, \varphi=1}^2 \left\{ -\frac{m_{\nu_\varpi} m_{\nu_\varrho}}{2e^2 m_W^4} E_8(x_{\nu_\varpi}, x_{\nu_\varrho}, x_{H_\phi^\pm}, x_{H_\varphi^\pm}) C_R^{H_\varphi^\pm \nu_\varpi \bar{l}_i} C_R^{H_\phi^\pm^* l_j \bar{\nu}_\varpi} C_L^{H_\phi^\pm \nu_\varrho \bar{l}_i} C_L^{H_\varphi^\pm^* l_i \bar{\nu}_\varrho} \right. \\
& + \frac{1}{4e^2 m_W^2} E_7(x_{\nu_\varpi}, x_{\nu_\varrho}, x_{H_\phi^\pm}, x_{H_\varphi^\pm}) \left[C_R^{H_\varphi^\pm \nu_\varpi \bar{l}_i} C_L^{H_\phi^\pm^* l_j \bar{\nu}_\varpi} C_L^{H_\phi^\pm \nu_\varrho \bar{l}_i} C_R^{H_\varphi^\pm^* l_i \bar{\nu}_\varrho} \right. \\
& + \left. C_R^{H_\varphi^\pm \nu_\varpi \bar{l}_i} C_L^{H_\phi^\pm^* l_j \bar{\nu}_\varpi} C_R^{H_\varphi^\pm \nu_\varrho \bar{l}_i} C_L^{H_\phi^\pm^* l_i \bar{\nu}_\varrho} \right] \left. \right\}, \\
B_3^L(n) = & \sum_{\beta, n=1}^8 \sum_{\rho, \sigma=1}^6 \frac{m_{\chi_\beta^0} m_{\chi_n^0}}{e^2 m_W^4} E_8(x_{\chi_\beta^0}, x_{\chi_n^0}, x_{\tilde{L}_\rho}, x_{\tilde{L}_\sigma}) \left[C_L^{\tilde{L}_\sigma \chi_\beta^0 \bar{l}_i} C_L^{\tilde{L}_\rho^* l_j \bar{\chi}_\beta^0} C_L^{\tilde{L}_\rho \chi_n^0 \bar{l}_i} C_L^{\tilde{L}_\sigma^* l_i \bar{\chi}_n^0} \right. \\
& - \frac{1}{2} C_L^{\tilde{L}_\sigma \chi_\beta^0 \bar{l}_i} C_L^{\tilde{L}_\rho^* l_j \bar{\chi}_\beta^0} C_L^{\tilde{L}_\sigma \chi_n^0 \bar{l}_i} C_L^{\tilde{L}_\rho^* l_i \bar{\chi}_n^0} \left. \right] \\
& + \sum_{\varpi, \varrho=1}^6 \sum_{\phi, \varphi=1}^2 \frac{m_{\nu_\varpi} m_{\nu_\varrho}}{e^2 m_W^4} E_8(x_{\nu_\varpi}, x_{\nu_\varrho}, x_{H_\phi^\pm}, x_{H_\varphi^\pm}) \left[C_L^{H_\varphi^\pm \nu_\varpi \bar{l}_i} C_L^{H_\phi^\pm^* l_j \bar{\nu}_\varpi} C_L^{H_\phi^\pm \nu_\varrho \bar{l}_i} C_L^{H_\varphi^\pm^* l_i \bar{\nu}_\varrho} \right. \\
& - \frac{1}{2} C_L^{H_\varphi^\pm \nu_\varpi \bar{l}_i} C_L^{H_\phi^\pm^* l_j \bar{\nu}_\varpi} C_L^{H_\varphi^\pm \nu_\varrho \bar{l}_i} C_L^{H_\phi^\pm^* l_i \bar{\nu}_\varrho} \left. \right], \\
B_4^L(n) = & \sum_{\beta, n=1}^8 \sum_{\rho, \sigma=1}^6 \frac{m_{\chi_\beta^0} m_{\chi_n^0}}{8e^2 m_W^4} E_8(x_{\chi_\beta^0}, x_{\chi_n^0}, x_{\tilde{L}_\rho}, x_{\tilde{L}_\sigma}) C_L^{\tilde{L}_\sigma \chi_\beta^0 \bar{l}_i} C_L^{\tilde{L}_\rho^* l_j \bar{\chi}_\beta^0} C_L^{\tilde{L}_\sigma \chi_n^0 \bar{l}_i} C_L^{\tilde{L}_\rho^* l_i \bar{\chi}_n^0} \\
& + \sum_{\varpi, \varrho=1}^6 \sum_{\phi, \varphi=1}^2 \frac{m_{\nu_\varpi} m_{\nu_\varrho}}{8e^2 m_W^4} E_8(x_{\nu_\varpi}, x_{\nu_\varrho}, x_{H_\phi^\pm}, x_{H_\varphi^\pm}) C_L^{H_\varphi^\pm \nu_\varpi \bar{l}_i} C_L^{H_\phi^\pm^* l_j \bar{\nu}_\varpi} C_L^{H_\varphi^\pm \nu_\varrho \bar{l}_i} C_L^{H_\phi^\pm^* l_i \bar{\nu}_\varrho}, \\
B_5^L(n) = & 0, \\
B_\beta^R(n) = & B_\beta^L(n)|_{L \leftrightarrow R}, \quad \beta = 1 \dots 5,
\end{aligned} \tag{31}$$

We also deduce the box-type contributions from virtual W-neutrino

$$\begin{aligned}
B_1^L(W) &= \sum_{\varpi, \varrho=1}^6 \frac{1}{e^2 m_W^2} \left[-\frac{\partial}{\partial x_W} E_2(x_W, x_{\nu_\varpi}, x_{\nu_\varrho}) C_L^{W l_j \bar{\nu}_\varpi} C_L^{W^* \nu_\varpi \bar{l}_i} C_L^{W^* \nu_\varrho \bar{l}_i} C_L^{W l_i \bar{\nu}_\varrho} \right. \\
&\quad \left. - 2 \frac{m_{\nu_\varpi} m_{\nu_\varrho}}{m_W^2} \frac{\partial}{\partial x_W} E_1(x_W, x_{\nu_\varpi}, x_{\nu_\varrho}) C_L^{W l_j \bar{\nu}_\varpi} C_L^{W^* \nu_\varrho \bar{l}_i} C_L^{W l_i \bar{\nu}_\varrho} C_L^{W^* \nu_\varpi \bar{l}_i} \right], \\
B_3^L(W) &= \sum_{\varpi, \varrho=1}^6 -\frac{7}{2} \frac{m_{\nu_\varpi} m_{\nu_\varrho}}{e^2 m_W^4} \frac{\partial}{\partial x_W} E_1(x_W, x_{\nu_\varpi}, x_{\nu_\varrho}) C_L^{W l_j \bar{\nu}_\varpi} C_L^{W^* \nu_\varrho \bar{l}_i} C_L^{W l_i \bar{\nu}_\varrho} C_L^{W^* \nu_\varpi \bar{l}_i}, \\
B_2^L(W) &= 0, \quad B_4^L(W) = \frac{1}{14} B_3^L(W), \quad B_5^L(W) = -\frac{1}{7} B_3^L(W), \\
B_1^R(W) &= 0, \quad B_\alpha^R(W) = B_\alpha^L(W)|_{L \leftrightarrow R}, \quad \alpha = 2 \dots 5,
\end{aligned} \tag{32}$$

With Eqs.(29)(31)(32), we formulate the coefficients $B_\beta^{L,R}$ as follows:

$$B_\beta^{L,R} = B_\beta^{L,R}(c) + B_\beta^{L,R}(n) + B_\beta^{L,R}(W), \quad (\beta = 1 \dots 5). \tag{33}$$

The decay widths for $l_j \rightarrow 3l_i$ can be calculated by evaluating the corresponding amplitudes,

$$\begin{aligned}
\Gamma(l_j \rightarrow 3l_i) &= \frac{e^4}{512\pi^3} m_{l_j}^5 \left\{ (|A_2^L|^2 + |A_2^R|^2) \left(\frac{16}{3} \ln \frac{m_{l_j}}{2m_{l_i}} - \frac{14}{9} \right) \right. \\
&\quad + (|A_1^L|^2 + |A_1^R|^2) - 2(A_1^L A_2^{R*} + A_2^L A_1^{R*} + A_2^L A_1^{R*} + A_1^L A_2^{R*}) + \frac{1}{6}(|B_1^L|^2 + |B_1^R|^2) \\
&\quad + \frac{1}{3}(|B_2^L|^2 + |B_2^R|^2) + \frac{1}{24}(|B_3^L|^2 + |B_3^R|^2) + 6(|B_4^L|^2 + |B_4^R|^2) + \frac{1}{12}(|B_5^L|^2 + |B_5^R|^2) \\
&\quad - \frac{1}{6}(B_2^L B_5^{L*} + B_2^R B_5^{R*} + A_1^L B_5^{L*} + A_1^R B_5^{R*} + B_5^R B_2^{R*} + B_5^L B_2^{L*} + B_5^R A_1^{R*} + B_5^L A_1^{L*}) \\
&\quad + \frac{1}{3}(A_2^R B_5^{L*} + A_2^L B_5^{R*} + B_5^R A_2^{L*} + B_5^L A_2^{R*}) - \frac{1}{6}(D_{LR} B_5^{L*} + D_{RL} B_5^{R*} + B_5^R D_{RL}^* + B_5^L D_{LR}^*) \\
&\quad - \frac{1}{2}(B_3^L B_4^{L*} + B_3^R B_4^{R*} + B_4^R B_3^{R*} + B_4^L B_3^{L*}) + \frac{1}{3}(A_1^L B_1^{L*} + A_1^R B_1^{R*} + A_1^L B_2^{L*} \\
&\quad + A_1^R B_2^{R*} + B_1^R A_1^{R*} + B_1^L A_1^{L*} + B_2^R A_1^{R*} + B_2^L A_1^{L*}) - \frac{2}{3}(A_2^R B_1^{L*} + A_2^L B_1^{R*} + A_2^L B_2^{R*} \\
&\quad + A_2^R B_2^{L*} + B_1^R A_2^{L*} + B_1^L A_2^{R*} + B_2^L A_2^{R*} + B_2^R A_2^{L*}) + \frac{1}{3} \left[2(|D_{LL}|^2 + |D_{RR}|^2) \right. \\
&\quad + (|D_{LR}|^2 + |D_{RL}|^2) + (B_1^L D_{LL}^* + B_1^R D_{RR}^* + B_2^L D_{LR}^* + B_2^R D_{RL}^* + D_{RR} B_1^{R*} \\
&\quad + D_{LL} B_1^{L*} + D_{RL} B_2^{R*} + D_{LR} B_2^{L*}) + 2(A_1^L D_{LL}^* + A_1^R D_{RR}^* + D_{RR} A_1^{R*} + D_{LL} A_1^{L*}) \\
&\quad + (A_1^L D_{LR}^* + A_1^R D_{RL}^* + D_{RL} A_1^{R*} + D_{LR} A_1^{L*}) - 4(A_2^R D_{LL}^* + A_2^L D_{RR}^* + D_{RR} A_2^{L*} \\
&\quad \left. \left. + D_{LL} A_2^{R*}) - 2(A_2^L D_{RL}^* + A_2^R D_{LR}^* + D_{LR} A_2^{R*} + D_{RL} A_2^{L*}) \right] \right\},
\end{aligned} \tag{34}$$

with

$$D_{LL} = \frac{D_L C_L^{Z l_i \bar{l}_i}}{m_Z^2}, \quad D_{RR} = D_{LL}|_{L \leftrightarrow R},$$

$$D_{LR} = \frac{D_L C_R^{Zl_i \bar{l}_i}}{m_Z^2}, \quad D_{RL} = D_{LR}|_{L \leftrightarrow R}. \quad (35)$$

Finally, the branching ratios of $l_j \rightarrow 3l_i$ are given by

$$Br(l_j \rightarrow 3l_i) = \frac{\Gamma(l_j \rightarrow 3l_i)}{\Gamma_{l_j}} \quad (36)$$

C. $\mu \rightarrow e + q\bar{q}$

The effective Lagrangian corresponding to the box-type diagrams shown in Fig.4 can be expressed as

$$T_{\text{box}} = e^2 \sum_{q=u,d} \bar{q} \gamma_\alpha q \bar{e} \gamma^\alpha (O_q^L P_L + O_q^R P_R) \mu. \quad (37)$$

with

$$O_q^{L,R} = O_q^{(n)L,R} + O_q^{(c)L,R} + O_q^{(W)L,R}(q = u, d). \quad (38)$$

$O_q(n)$ represent the contributions from the virtual neutral Fermion diagrams in the first line of Fig.4.

$$\begin{aligned} O_q^L(n) = & \sum_{\beta,n=1}^8 \sum_{l=1}^6 \left\{ \frac{1}{8e^2 m_W^2} E_7(x_{\chi_\beta^0}, x_{\chi_n^0}, x_{\tilde{L}_\alpha}, x_{\tilde{Q}_l}) \left[C_L^{\tilde{L}_\alpha \mu \tilde{\chi}_\beta^0} C_R^{\tilde{L}_\alpha \chi_n^0 \bar{e}} C_R^{\tilde{Q}_l \chi_\beta^0 \bar{q}} C_L^{\tilde{Q}_l q \tilde{\chi}_n^0} \right. \right. \\ & - C_L^{\tilde{L}_\alpha \mu \tilde{\chi}_\beta^0} C_R^{\tilde{L}_\alpha \chi_n^0 \bar{e}} C_R^{\tilde{Q}_l q \tilde{\chi}_\beta^0} C_L^{\tilde{Q}_l \chi_n^0 \bar{q}} \left. \right] \\ & - \frac{m_{\chi_\beta^0} m_{\chi_n^0}}{4e^2 m_W^4} E_8(x_{\chi_\beta^0}, x_{\chi_n^0}, x_{\tilde{L}_\alpha}, x_{\tilde{Q}_l}) \left[C_L^{\tilde{L}_\alpha \mu \tilde{\chi}_\beta^0} C_R^{\tilde{L}_\alpha \chi_n^0 \bar{e}} C_L^{\tilde{Q}_l \chi_\beta^0 \bar{q}} C_R^{\tilde{Q}_l q \tilde{\chi}_n^0} \right. \\ & \left. \left. - C_L^{\tilde{L}_\alpha \mu \tilde{\chi}_\beta^0} C_R^{\tilde{L}_\alpha \chi_n^0 \bar{e}} C_L^{\tilde{Q}_l q \tilde{\chi}_\beta^0} C_R^{\tilde{Q}_l \chi_n^0 \bar{q}} \right] \right\}, \\ O_q^R(n) = & O_q^L(n)|_{L \leftrightarrow R}, \quad (q = u, d). \end{aligned} \quad (39)$$

Correspondingly, the virtual charged Fermion diagrams give contributions denoted by $O_q(c)$.

$$\begin{aligned} O_d^L(c) = & \sum_{\eta,\theta=1}^2 \sum_{\sigma,l=1}^6 \left[\frac{1}{8e^2 m_W^2} E_7(x_{\chi_\eta^\pm}, x_{\chi_\theta^\pm}, x_{\tilde{\nu}_\sigma}, x_{\tilde{U}_l^+}) C_L^{\tilde{\nu}_\sigma \mu \tilde{\chi}_\eta^\pm} C_R^{\tilde{\nu}_\sigma \chi_\theta^\pm \bar{e}} C_R^{\tilde{U}_l^+ \chi_\eta^\pm \bar{d}} C_L^{\tilde{U}_l^+ d \tilde{\chi}_\theta^\pm} \right. \\ & \left. - \frac{m_{\chi_\eta^\pm} m_{\chi_\theta^\pm}}{4e^2 m_W^4} E_8(x_{\chi_\eta^\pm}, x_{\chi_\theta^\pm}, x_{\tilde{\nu}_\sigma}, x_{\tilde{U}_l^+}) C_L^{\tilde{\nu}_\sigma \mu \tilde{\chi}_\eta^\pm} C_R^{\tilde{\nu}_\sigma \chi_\theta^\pm \bar{e}} C_L^{\tilde{U}_l^+ \chi_\eta^\pm \bar{d}} C_R^{\tilde{U}_l^+ d \tilde{\chi}_\theta^\pm} \right], \end{aligned}$$

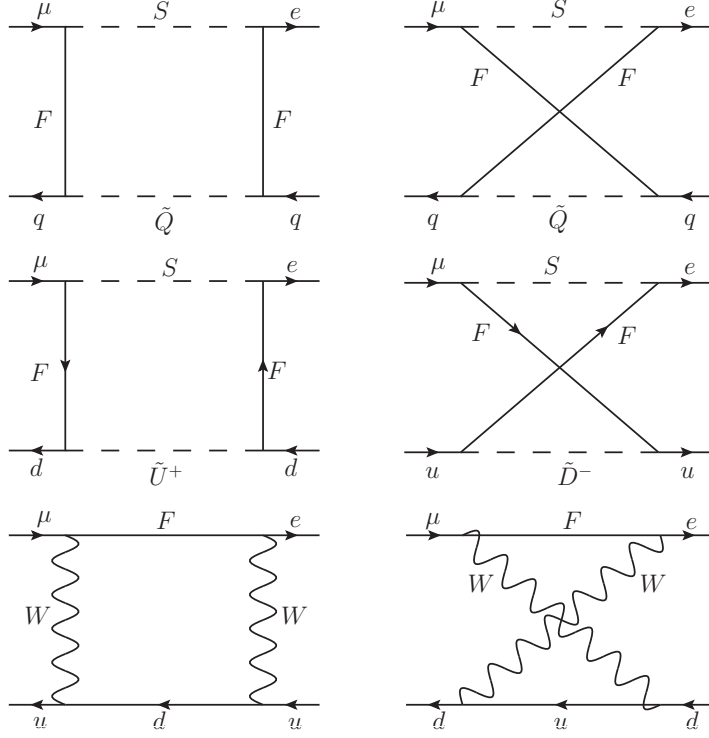


FIG. 4: The box-type diagrams for $\mu \rightarrow e + q\bar{q}$, with F representing Dirac(Majorana) particles.

$$\begin{aligned}
O_u^L(c) &= \sum_{\eta, \theta=1}^2 \sum_{\sigma, l=1}^6 \left[\frac{-1}{8e^2 m_W^2} E_7(x_{\chi_\eta^\pm}, x_{\chi_\theta^\pm}, x_{\tilde{\nu}_\sigma}, x_{\tilde{D}_l^-}) C_L^{\tilde{\nu}_\sigma \mu \bar{\chi}_\eta^\pm} C_R^{\tilde{\nu}_\sigma \chi_\theta^\pm \bar{e}} C_R^{\tilde{D}_l^- \chi_\eta^\pm \bar{u}} C_L^{\tilde{D}_l^- u \bar{\chi}_\theta^\pm} \right. \\
&\quad \left. + \frac{m_{\chi_\eta^\pm} m_{\chi_\theta^\pm}}{4e^2 m_W^4} E_8(x_{\chi_\eta^\pm}, x_{\chi_\theta^\pm}, x_{\tilde{\nu}_\sigma}, x_{\tilde{D}_l^-}) C_L^{\tilde{\nu}_\sigma \mu \bar{\chi}_\eta^\pm} C_R^{\tilde{\nu}_\sigma \chi_\theta^\pm \bar{e}} C_L^{\tilde{D}_l^- \chi_\eta^\pm \bar{u}} C_R^{\tilde{D}_l^- u \bar{\chi}_\theta^\pm} \right], \\
O_q^R(c) &= O_q^L(c)|_{L \leftrightarrow R}.
\end{aligned} \tag{40}$$

Furthermore, the virtual W produces corrections through the diagrams in the last line of Fig.4.

$$\begin{aligned}
O_d^L(W) &= \sum_{\delta=1}^6 -\frac{1}{2e^2} \frac{\partial}{\partial x_W} E_2(x_W, x_{\nu_\delta}, x_u) C_L^{W \mu \bar{\nu}_\delta} C_L^{W^* \nu_\delta \bar{e}} C_L^{W^* u \bar{d}} C_L^{W d \bar{u}}, \\
O_u^L(W) &= \sum_{\delta=1}^6 \frac{2}{e^2} \frac{\partial}{\partial x_W} E_2(x_W, x_{\nu_\delta}, x_d) C_L^{W^* \mu \bar{\nu}_\delta} C_L^{W \nu_\delta \bar{e}} C_L^{W^* d \bar{u}} C_L^{W u \bar{d}}, \\
O_d^R(W) &= O_u^R(W) = 0.
\end{aligned} \tag{41}$$

Starting from the effective Lagrangian describing $\mu - e$ conversion processes at the quark level, one can determine the $\mu - e$ conversion rate within a nucleus [29]:

$$\text{CR}(\mu \rightarrow e : \text{Nucleus})$$

$$\begin{aligned}
&= 4\alpha^5 \frac{Z_{\text{eff}}^4}{Z} |F(q^2)|^2 m_\mu^5 \left[|Z(A_1^L - A_2^R) - (2Z + N)\bar{O}_u^L - (Z + 2N)\bar{O}_d^L|^2 \right. \\
&\quad \left. + |Z(A_1^R - A_2^L) - (2Z + N)\bar{O}_u^R - (Z + 2N)\bar{O}_d^R|^2 \right] \frac{1}{\Gamma_{\text{capt}}}, \tag{42}
\end{aligned}$$

with

$$\begin{aligned}
T_{3L}^u &= \frac{1}{2}, \quad T_{3L}^d = -\frac{1}{2}, \quad T_{3R}^u = T_{3R}^d = 0, \quad Q_{em}^u = \frac{2}{3}, \quad Q_{em}^d = -\frac{1}{3}, \\
Z_{L,R}^q &= T_{3L,R}^q - Q_{em}^q s_w^2, \quad (q = u, d), \\
\bar{O}_q^L &= O_q^L + \frac{Z_L^q + Z_R^q}{2} \frac{D_L}{m_Z^2 s_w^2 c_w^2}, \quad (s_w = \sin \theta_w, \quad c_w = \cos \theta_w), \\
\bar{O}_q^R &= \bar{O}_q^L|_{L \leftrightarrow R}, \quad (q = u, d). \tag{43}
\end{aligned}$$

In this context, Z and N correspond to the number of protons and neutrons comprising a nucleus, whereas Z_{eff} denotes the effective atomic charge, as ascertained in the referenced studies [30, 31]. $F(q^2)$ represents the nuclear form factor, and Γ_{capt} is the total muon capture rate. For an array of distinct nuclei, the respective values of Z_{eff} , $F(q^2 \simeq -m_\mu^2)$, and Γ_{capt} have been compiled in Table II, in accordance with the methodology outlined in Ref. [32].

TABLE II: The values of Z_{eff} , $F(q^2 \simeq -m_\mu^2)$ and $\Gamma_{(\text{capt})}$ for different nuclei

$\frac{A}{Z}\text{Nucleus}$	Z_{eff}	$F(q^2 \simeq -m_\mu^2)$	$\Gamma_{\text{capt}}(\text{GeV})$
$\frac{48}{22}\text{Ti}$	17.6	0.54	1.70422×10^{-18}
$\frac{197}{79}\text{Au}$	33.5	0.16	8.59868×10^{-18}
$\frac{207}{82}\text{Pb}$	34.0	0.15	8.84868×10^{-18}

IV. NUMERICAL RESULTS

In this section, we analyze the numerical results and consider the experimental constraints. In order to obtain reasonable numerical results, a number of sensitive parameters need to be investigated from those used. Given that experimental constraints from the $l_j \rightarrow l_i \gamma$ processes tightly constrain the parameter space of the N-B-LSSM, it is crucial to take into account the impacts of $l_j \rightarrow l_i \gamma$ on LFV when analyzing $l_j \rightarrow 3l_i$ and $\mu \rightarrow e + q\bar{q}$ processes. If the strict conditions set by the $l_j \rightarrow l_i \gamma$ processes are satisfied, it is reasonable to expect that the constraints from other related LFV processes will also be satisfied.

Several experimental restrictions are considered, including:

1. The lightest CP-even Higgs h^0 mass is around 125.20 ± 0.11 GeV [9, 33, 34].
2. According to the latest data from the LHC [35–40], the scalar lepton mass is greater than 700 GeV, the chargino mass is greater than 1100 GeV, and the scalar quark mass is greater than 1500 GeV.
3. The new angle $\tan \beta_\eta$ constrained by the LHC should be less than 1.5 [41].
4. The Z' boson mass is larger than 5.1 TeV [42].
5. The ratio between $M_{Z'}$ and its gauge $M_{Z'}/g_B \geq 6$ TeV [43, 44].
6. The limitations from Charge and Color Breaking (CCB), neutrino experiment data and muon anomalous magnetic dipole moment are also taken into account [45–50].

The Yukawa couplings of neutrinos $Y_{\nu ij}$ ($i, j = 1, 2, 3$) are at the order of $10^{-8} \sim 10^{-6}$ and its effects on the LFV processes are small and usually negligible. Incorporating the experimental requirements, we compile and analyse extensive data, generating one-dimensional plots and scatter plots to illustrate the correlations between various parameters and branching ratios. Through the analysis of these plots in conjunction with the experimental constraints on branching ratios, a viable parameter space is identified to explain LFV.

Considering these limitations, we adopt the following parameters in the numerical calculation:

$$\begin{aligned}
\lambda_2 &= -0.25, \quad \kappa = 0.1, \quad \tan \beta_\eta = 0.9, \quad Y_{Xii} = 0.5, \\
T_\kappa &= -2.5 \text{ TeV}, \quad T_\lambda = T_{\lambda_2} = 1 \text{ TeV}, \quad M_1 = 0.4 \text{ TeV}, \\
M_{BL} &= 1 \text{ TeV}, \quad M_{BB'} = 0.1 \text{ TeV}, \quad M_{\nu ii}^2 = 2.5 \text{ TeV}^2, \\
T_{u ii} &= 1 \text{ TeV}, \quad T_{d ii} = 1 \text{ TeV}, \quad T_{X ii} = -4 \text{ TeV}, (i = 1, 2, 3).
\end{aligned} \tag{44}$$

To facilitate the numerical investigation, we employ the parameter relationships and analyze their variations in the subsequent numerical analysis:

$$\begin{aligned}
&\tan \beta, \quad g_B, \quad g_{YB}, \quad \lambda, \quad v_S, \quad M_2, \quad M_{\nu ii}^2 = M_\nu^2, \quad M_{Li i}^2 = M_L^2, \\
&M_{E ii}^2 = M_E^2, \quad M_{\nu ij}^2 = M_{\nu ji}^2, \quad M_{L ij}^2 = M_{L ji}^2, \quad M_{E ij}^2 = M_{E ji}^2, \\
&T_{e ii} = T_e, \quad T_{\nu ii} = T_\nu, \quad T_{e ij} = T_{e ji}, \quad T_{\nu ij} = T_{\nu ji}, (i, j = 1, 2, 3, i \neq j).
\end{aligned} \tag{45}$$

If no special case exists, the non-diagonal elements of the parameters are assumed to be zero.

A. $l_j \rightarrow l_i \gamma$

LFV is closely associated with NP, and the branching ratio of the process $\mu \rightarrow e \gamma$ is subject to stringent experimental constraints. The latest experimental upper limit on its branching ratio is 4.2×10^{-13} at 90% confidence level. At this subsection, the chosen parameters are $M_2 = 1.2$ TeV, $v_S = 4$ TeV, $\lambda = 0.4$, $T_\nu = 1$ TeV, $M_E^2 = 1.5$ TeV².

1. $\mu \rightarrow e \gamma$

We conduct numerical calculations for $\text{Br}(\mu \rightarrow e \gamma)$, and depict the impacts of various parameters in Fig.5. The gray area indicates the region satisfying the experimental upper limit.

With the parameters $g_{YB} = 0.2$, $g_B = 0.6$, $T_e = 1$ TeV, $M_L^2 = 0.16$ TeV², the variation of $\text{Br}(\mu \rightarrow e \gamma)$ with respect to $T_{\nu 12}$ is depicted in Fig.5(a). The red line corresponds to $\tan \beta = 30$ and the blue line corresponds to $\tan \beta = 20$. $\tan \beta$ represents the ratio of the VEVs of two Higgs doublets ($\tan \beta = v_u/v_d$), and it influences particle masses by directly affecting v_u and v_d . $\tan \beta$ is closely associated with the mass matrixes of chargino, neutralino, slepton and sneutrino, particularly their non-diagonal elements. In the N-B-LSSM, nearly all contributions to LFV processes are impacted by $\tan \beta$. As a highly sensitive parameter, $\tan \beta$ has a significant effect on numerical results. It can be observed from Fig.5(a) that $\text{Br}(\mu \rightarrow e \gamma)$ rises as $\tan \beta$ increases. As a non-diagonal element of the sneutrino mass matrix, $T_{\nu 12}$ influences the masses and mixing of sneutrino. In the range from 20 GeV-500 GeV, $\text{Br}(\mu \rightarrow e \gamma)$ increases with the augment of $T_{\nu 12}$. Both $\tan \beta$ and $T_{\nu 12}$ are sensitive parameters, and since the upper limit for $\text{Br}(\mu \rightarrow e \gamma)$ is small, it is easy to exceed that upper limit in the N-B-LSSM.

Supposing $\tan \beta = 50$, $g_B = 0.6$, $T_e = 1$ TeV, $M_L^2 = 0.16$ TeV², we represent the variation of $\text{Br}(\mu \rightarrow e \gamma)$ with M_{L12}^2 using red line ($g_{YB} = 0.25$) and blue line ($g_{YB} = 0.3$) in Fig.5(b). g_{YB} is the mixing gauge coupling constant of $U(1)_Y$ group and $U(1)_{B-L}$ group, it describes the interactions and mixing effects between two $U(1)$ gauge groups, which is a new parameter that goes beyond MSSM and can bring new effects. M_{L12}^2 is the flavour mixing parameter that appears in the mass matrixes of the slepton, CP-even sneutrino and CP-odd sneutrino. We can clearly see that these two lines increase with M_{L12}^2 . Overall the red line is larger than the blue line, the blue line as a whole and the red line in the range $120 \text{ GeV}^2 < M_{L12}^2 < 2100 \text{ GeV}^2$ are located in the gray area that satisfies the limits of the

experiment, and the rest of the red line goes beyond the gray area.

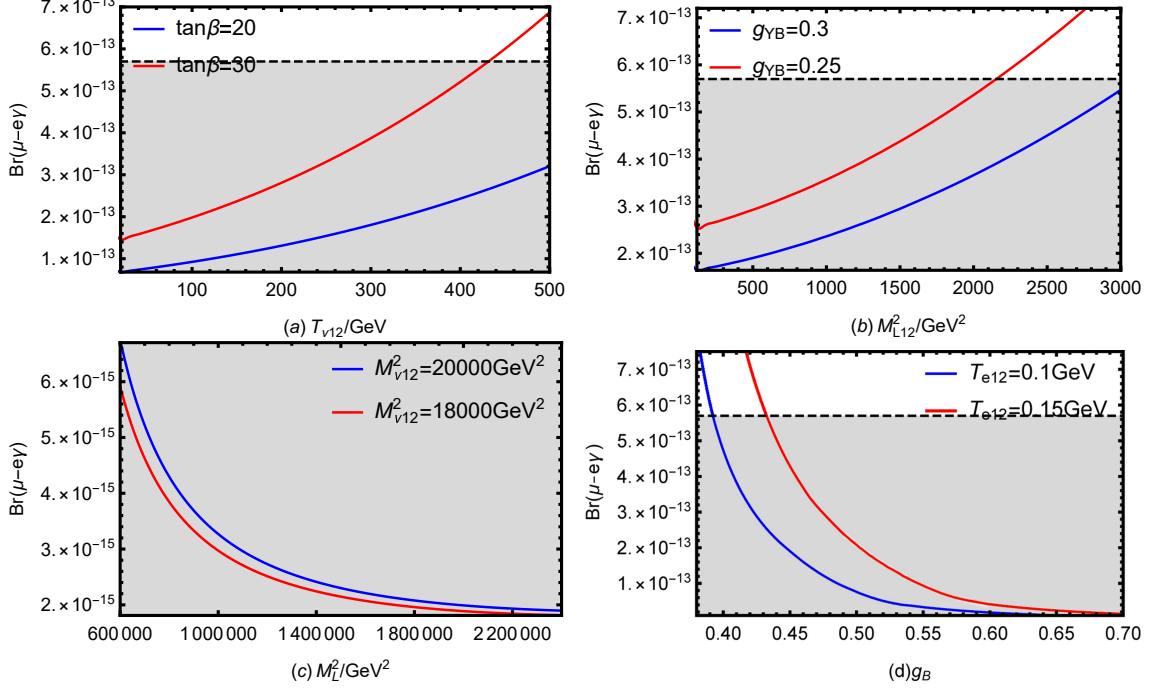


FIG. 5: $\text{Br}(\mu \rightarrow e\gamma)$ schematic diagrams affected by different parameters, the gray area satisfies the experimental upper limit. Fig.5(a) shows the relationship between $T_{\nu 12}$ and $\text{Br}(\mu \rightarrow e\gamma)$ with the red line representing $\tan \beta=30$ and the blue line representing $\tan \beta=20$. Fig.5(b) shows the relationship between M_{L12}^2 and $\text{Br}(\mu \rightarrow e\gamma)$ with the red line representing $g_{YB} = 0.25$ and the blue line representing $g_{YB} = 0.3$. Fig.5(c) shows the relationship between M_L^2 and $\text{Br}(\mu \rightarrow e\gamma)$ with the red line representing $M_{\nu 12}^2 = 1.8 \times 10^4 \text{ GeV}^2$ and the blue line representing $M_{\nu 12}^2 = 2 \times 10^4 \text{ GeV}^2$. Fig.5(d) shows the relationship between g_B and $\text{Br}(\mu \rightarrow e\gamma)$ with the red line representing $T_{e12} = 0.15 \text{ GeV}$ and the blue line representing $T_{e12} = 0.1 \text{ GeV}$.

Based on $\tan \beta = 25$, $g_B = 0.3$, $g_{YB} = 0.1$, $T_e = 1 \text{ TeV}$, the blue line in Fig.5(c) corresponds to $M_{\nu 12}^2 = 2 \times 10^4 \text{ GeV}^2$ and the red line corresponds to $M_{\nu 12}^2 = 1.8 \times 10^4 \text{ GeV}^2$. These two lines show the trend of $\text{Br}(\mu \rightarrow e\gamma)$ with the change of M_L^2 at different values of $M_{\nu 12}^2$. As M_L^2 increases, both lines show a gradual decrease in $\text{Br}(\mu \rightarrow e\gamma)$, and the two lines are very close to each other in the whole M_L^2 range. The similarity in the trends could suggest that M_L^2 exhibits greater sensitivity compared to $M_{\nu 12}^2$, this is because M_L^2 impacts the masses of both slepton and sneutrino, while $M_{\nu 12}^2$ only influences sneutrino masses.

Setting $\tan \beta = 25$, $g_{YB} = 0.1$, $T_e = 1 \text{ TeV}$, $M_L^2 = 0.16 \text{ TeV}^2$, we study the effect of the parameter g_B on $\text{Br}(\mu \rightarrow e\gamma)$ in Fig.5(d), where the red and blue lines represent the cases of

$T_{e12} = 0.15$ GeV and $T_{e12} = 0.1$ GeV, respectively. g_B is the coupling constant of the gauge group. g_B appears in almost all mass matrixes and determines how bosons interact with fermions, Higgs field and other particles. So it is clear that g_B is a sensitive parameter. As depicted in Fig.5(d), the value of $\text{Br}(\mu \rightarrow e\gamma)$ decreases with an increase in parameter g_B . There is T_{e12} as a non-diagonal element in the slepton mass squared matrix, which influences the results through neutralino-slepton contributions. It is evident that despite a change of only 0.05 GeV in T_{e12} , it has led to a significant difference in $\text{Br}(\mu \rightarrow e\gamma)$. Specifically, when T_{e12} increase from 0.1 GeV to 0.15 GeV, $\text{Br}(\mu \rightarrow e\gamma)$ increases for the same value of g_B .

2. $\tau \rightarrow \mu\gamma$

The upper bound of $\text{Br}(\tau \rightarrow \mu\gamma)$ experiment is 4.2×10^{-8} , which is nearly 5 orders of magnitude larger than the experimental upper bound of $\text{Br}(\mu \rightarrow e\gamma)$. First, we set the parameters $g_{YB} = 0.1$, $g_B = 0.3$, $M_L^2 = 0.16$ TeV². Next, we perform random scattering with parameters and ranges shown in Table III. Among these parameters, there are both sensitive and insensitive parameters. Based on the randomly scanned data, we draw Fig.6 to find the rules. In order to observe the numerical patterns more clearly and to facilitate the analysis of the results, we divide the numerical data obtained from the random scattering points into different ranges. We use \blacklozenge ($0 < \text{Br}(\tau \rightarrow \mu\gamma) < 2 \times 10^{-9}$), \blacktriangle ($2 \times 10^{-9} \leq \text{Br}(\tau \rightarrow \mu\gamma) < 1.7 \times 10^{-8}$), \bullet ($1.7 \times 10^{-8} \leq \text{Br}(\tau \rightarrow \mu\gamma) < 4.4 \times 10^{-8}$) to denote the results.

The relationship between $\tan\beta$ and M_{E23}^2 is shown in Fig.6(a). M_{E23}^2 is a non-diagonal element that appears in the slepton mass matrix and affects the numerical results by influencing the slepton mixing and masses. Fig.6(a) as a whole presents a triangle shape gradually shrinking from the top left to the bottom right, with data points densely distributed in the lower left corner and almost no points in the upper right corner. \blacklozenge are mainly distributed in the region of $M_{E23}^2 < 2 \times 10^4$ GeV² and cover the whole range of $\tan\beta$ (from 5 to 50), with a relatively even distribution and no obviously downward trend. The M_{E23}^2 distribution of \blacktriangle ranges from about 1×10^4 GeV² to 4×10^4 GeV². \blacktriangle density gradually decreases as $\tan\beta$ increases, suggesting that fewer data satisfy this range for larger value of $\tan\beta$. \bullet are concentrated in the high M_{E23}^2 region, ranging from about 2×10^4 GeV² to 1×10^5 GeV². The number of \bullet decreases rapidly with the increase of $\tan\beta$, and especially after $\tan\beta > 20$. The maximum value of M_{E23}^2 decreases significantly, showing a steep negative correlation. The reason for this trend may be due to the existence of a non-linear relationship between the parameters, where an increase in $\tan\beta$ imposes a stronger restriction on M_{E23}^2 , resulting

TABLE III: Scanning parameters for Fig.6

Parameters	Min	Max
M_ν^2/GeV^2	1×10^5	2×10^6
M_{E23}^2/GeV^2	0	10^5
T_e/GeV	-2500	2500
$T_{\nu 23}/\text{GeV}$	-500	500
$\tan \beta$	5	50
g_B	0.3	0.6

in a rapid decrease in the value of M_{E23}^2 , which leads to a gradual convergence of the data points into the lower M_{E23}^2 region, and in addition $\text{Br}(\tau \rightarrow \mu\gamma)$ imposes tighter constraints on the parameter space, prohibiting the co-existence of high $\tan \beta$ and high M_{E23}^2 .

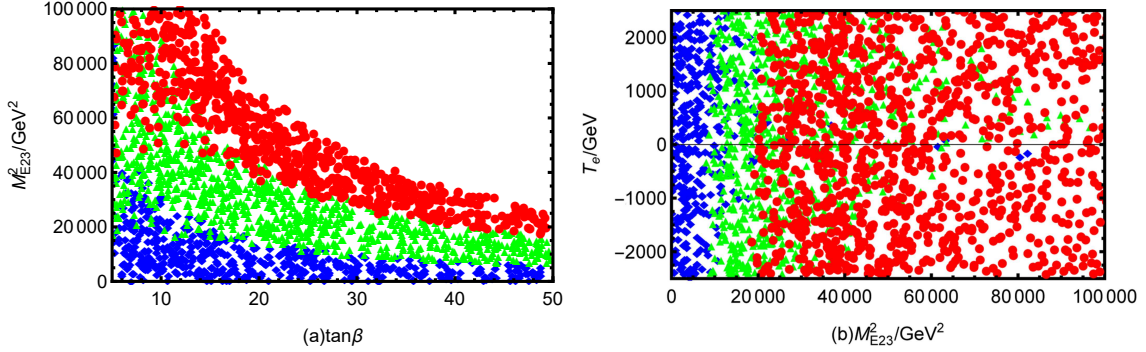


FIG. 6: Under the constraint of $\text{Br}(\tau \rightarrow \mu\gamma)$ process, a reasonable parameter space is selected for random scattering, and the marking of the scattering points represents: \blacklozenge ($0 < \text{Br}(\tau \rightarrow \mu\gamma) < 2 \times 10^{-9}$), \blacktriangle ($2 \times 10^{-9} \leq \text{Br}(\tau \rightarrow \mu\gamma) < 1.7 \times 10^{-8}$), \bullet ($1.7 \times 10^{-8} \leq \text{Br}(\tau \rightarrow \mu\gamma) < 4.4 \times 10^{-8}$).

The variation of T_e with M_{E23}^2 is plotted in Fig.6(b). \blacklozenge are concentrated in the low M_{E23}^2 , \blacktriangle are distributed in the middle region, and \bullet are concentrated in the high M_{E23}^2 region, showing a trend of distribution from left to right, and the range of data points expands gradually with the change of color. Point of all colors are relatively uniformly distributed over T_e , with a range that almost completely cover from -2500GeV to 2500GeV . T_e is also related to the slepton mass matrix, and we can analyse that T_e does not strongly influence the $\text{Br}(\tau \rightarrow \mu\gamma)$ compared to M_{E23}^2 . In summary, Fig.6(b) is symmetric about $T_e = 0$ GeV and the value of $\text{Br}(\tau \rightarrow \mu\gamma)$ becomes larger when the non-diagonal element M_{E23}^2 as the

flavor mixing parameter is increased.

3. $\tau \rightarrow e\gamma$

Similar to $\tau \rightarrow \mu\gamma$, $\tau \rightarrow e\gamma$ also has a large branching ratio, and the experimental upper bound is 3.3×10^{-8} . We study the influence of T_{e13} , g_B , M_L^2 and $\tan\beta$ on $\text{Br}(\tau \rightarrow e\gamma)$ in Fig.7.

Using the parameters $g_{YB} = 0.1$, $\tan\beta = 25$, $T_e = 1 \text{ TeV}$, $M_L^2 = 0.16 \text{ TeV}^2$, Fig.7(a) shows the relationship between $\text{Br}(\tau \rightarrow e\gamma)$ and T_{e13} for the two scenarios $g_B = 0.4$ (the blue line) and $g_B = 0.5$ (the red line), respectively. The parameter T_{e13} refers to one of the trilinear terms related to the soft supersymmetry breaking associated with the lepton Yukawa coupling. Whether $g_B = 0.4$ or $g_B = 0.5$, $\text{Br}(\tau \rightarrow e\gamma)$ increases with T_{e13} , and the increase is very significant over large T_{e13} ranges. To be specific, $\text{Br}(\tau \rightarrow e\gamma)$ increases faster with T_{e13} for $g_B = 0.4$. When T_{e13} is small (less than 100 GeV), the value of $\text{Br}(\tau \rightarrow e\gamma)$ is very low and close to zero. As T_{e13} exceeds 100 GeV, $\text{Br}(\tau \rightarrow e\gamma)$ begins to grow significantly. In contrast, when $g_B = 0.5$, the growth rate of $\text{Br}(\tau \rightarrow e\gamma)$ is significantly slower than that for $g_B = 0.4$. It can be concluded that the size of g_B affects the growth rate of the branching ratio. A reduction in the parameter g_B leads to a diminished contribution from the diagonal matrix elements, thereby indirectly enhancing the relative influence of the non-diagonal terms. Conversely, a larger g_B suppresses this growth effect, keeping the branching ratio well below the experimental upper limit.

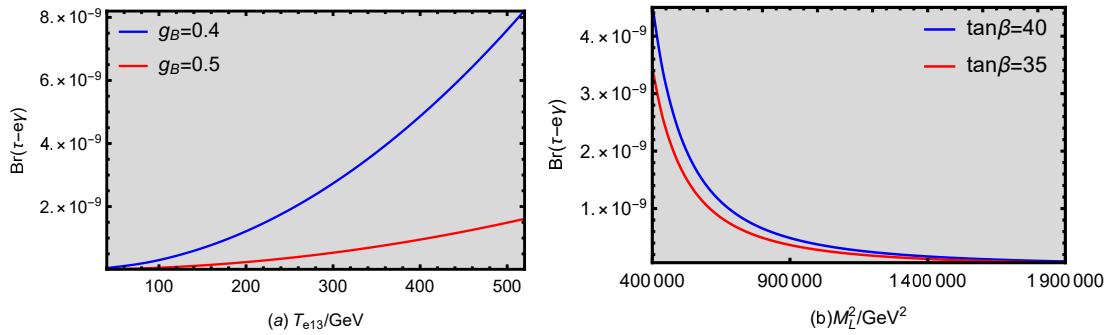


FIG. 7: $\text{Br}(\tau \rightarrow e\gamma)$ schematic diagrams affected by different parameters, the gray area satisfies the experimental upper limit. Fig.7(a) shows the relationship between T_{e13} and $\text{Br}(\tau \rightarrow e\gamma)$ with the red line representing $g_B = 0.5$ and the blue line representing $g_B = 0.4$. Fig.7(b) shows the relationship between M_L^2 and $\text{Br}(\tau \rightarrow e\gamma)$ with the red line representing $\tan\beta = 35$ and the blue line representing $\tan\beta = 40$.

Let $g_{YB} = 0.1$, $g_B = 0.3$, $T_e = 1$ TeV, $T_{\nu ij} = 0.5$ TeV, $M_{Lij}^2 = 0.016$ TeV² ($i, j = 1, 2, 3$, $i \neq j$) in Fig.7(b), the trend of $\text{Br}(\tau \rightarrow e\gamma)$ with M_L^2 is shown and the effect of $\tan\beta = 35$ (red line) and $\tan\beta = 40$ (blue line) on the branching ratio is compared. As M_L^2 increases, $\text{Br}(\tau \rightarrow e\gamma)$ decreases significantly and gradually tends to zero, with the decrease being more pronounced in the low M_L^2 region ($4 \times 10^5 \text{ GeV}^2 \leq M_L^2 < 9 \times 10^5 \text{ GeV}^2$) and flattening out at high M_L^2 region ($9 \times 10^5 \text{ GeV}^2 \leq M_L^2 < 1.9 \times 10^6 \text{ GeV}^2$). An increasing in M_L^2 directly suppresses the amplitude of the lepton transition process, because M_L^2 presents in the diagonal elements of the slepton and sneutrino mass matrices. As M_L^2 increases, the mass eigenvalues of the particles also increase, and these mass eigenvalues appear in the denominators of the propagators. Larger mass eigenvalues weaken the transition amplitudes, leading to a decrease in the branching ratio. The branching ratio at $\tan\beta = 40$ is consistently higher than that at $\tan\beta = 35$ for the same M_L^2 , and this difference is more obvious in the smaller M_L^2 region.

B. $l_j \rightarrow 3l_i$

In this subsection, we numerically investigate the LFV processes $l_j \rightarrow 3l_i$ under the assumption of $T_e = 1$ TeV. These processes are closely related to $l_j \rightarrow l_i\gamma$. Line graphs and scatter plots are drawn from the data obtained.

1. $\mu \rightarrow 3e$

$\text{Br}(\mu \rightarrow 3e)$ is the strictest branching ratio of LFV processes $l_j \rightarrow 3l_i$ and the experiment upper bound is 1.0×10^{-12} . In order to clearly find the sensitive parameters affecting $\mu \rightarrow 3e$, we plot Fig.8 for different parameters.

We set the parameters $g_{YB} = 0.02$, $\lambda = 0.4$, $M_2 = 1.2$ TeV, $v_S = 4$ TeV, $T_\nu = 1$ TeV, $T_{e12} = 3 \times 10^{-4}$ TeV, $M_L^2 = 0.16$ TeV², $M_E^2 = 1.5$ TeV² in Fig.8(a). It shows the variation of $\text{Br}(\mu \rightarrow 3e)$ with $\tan\beta$, where the lines correspond to different g_B values (the blue line corresponds to $g_B=0.3$, the red line corresponds to $g_B=0.6$). It can be observed that $\text{Br}(\mu \rightarrow 3e)$ gradually decreases as $\tan\beta$ increases. Moreover, for the same value of $\tan\beta$, $\text{Br}(\mu \rightarrow 3e)$ at $g_B=0.6$ is smaller than that at $g_B=0.3$, this indicates that an increase in the value of g_B also leads to a decrease in $\text{Br}(\mu \rightarrow 3e)$.

In the case of $\tan\beta = 25$, $g_B = 0.3$, $\lambda = 0.4$, $v_S = 4$ TeV, $T_\nu = 1$ TeV, $T_{e12} = 1 \times 10^{-4}$ TeV, $M_L^2 = 0.16$ TeV², $M_E^2 = 1.5$ TeV², we plot $\text{Br}(\mu \rightarrow 3e)$ varying with g_{YB} in

Fig.8(b), where the blue line is $M_2 = 1200$ GeV and the red line is $M_2 = 2000$ GeV. M_2 affects the mass matrixes of the neutralino and Chargino. At the same g_{YB} , the branching ratio corresponding to the larger M_2 is significantly higher than that of the smaller M_2 . g_{YB} is a sensitive parameter, $\text{Br}(\mu \rightarrow 3e)$ rises rapidly with g_{YB} . This trend reflects the fact that g_{YB} enhances the interaction strength of LFV process, while the increase of M_2 attenuates the inhibitory effect of the new physics particles masses on the propagation process, both of which together lead to the branching ratio growing in a nonlinear manner.

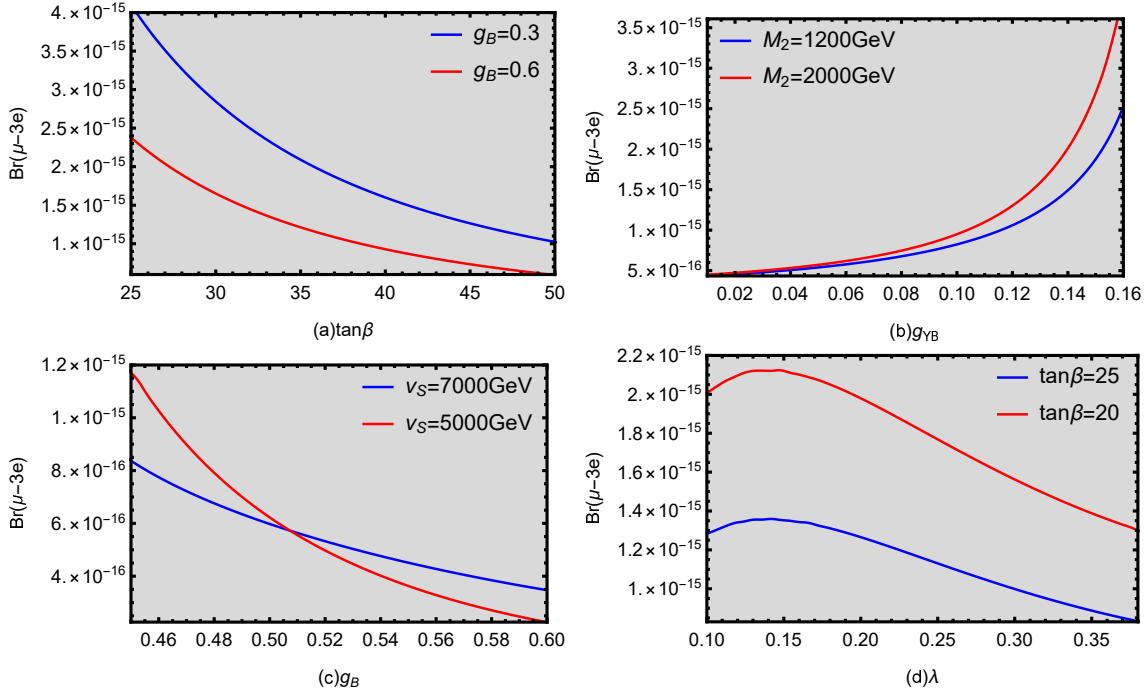


FIG. 8: $\text{Br}(\mu \rightarrow 3e)$ schematic diagrams affected by different parameters, the gray area satisfies the experimental upper limit. Fig.8(a) shows the relationship between $\tan\beta$ and $\text{Br}(\mu \rightarrow 3e)$ with the red line representing $g_B=0.6$ and the blue line representing $g_B=0.3$. Fig.8(b) shows the relationship between g_{YB} and $\text{Br}(\mu \rightarrow 3e)$ with the red line representing $M_2 = 2000$ GeV and the blue line representing $M_2 = 1200$ GeV. Fig.8(c) shows the relationship between g_B and $\text{Br}(\mu \rightarrow 3e)$ with the red line representing $v_S = 5000$ GeV and the blue line representing $v_S = 7000$ GeV. Fig.5(d) shows the relationship between λ and $\text{Br}(\mu \rightarrow 3e)$ with the red line representing $\tan\beta = 20$ and the blue line representing $\tan\beta = 25$.

$\tan\beta = 25$, $g_{YB} = 0.1$, $\lambda = 0.4$, $M_2 = 1.2$ TeV, $T_\nu = 1$ TeV, $T_{e12} = 1 \times 10^{-4}$ TeV, $M_L^2 = 0.16$ TeV², $M_E^2 = 1.5$ TeV² are set to study the relationship between $\text{Br}(\mu \rightarrow 3e)$ and g_B in Fig.8(c). The lines are divided into two cases corresponding to $v_S = 5000$ GeV (red line)

and $v_S = 7000$ GeV (blue line). v_S is the VEV of S and appears in the diagonal elements of CP-even Higgs mass squared matrix. More importantly, v_S affects the mass of the lightest neutralino through $m_{\tilde{\chi}_1\tilde{\chi}_2} = -\frac{1}{\sqrt{2}}\lambda_2 v_S$. In the $g_B < 0.5$ region, the red line is higher than the blue line. In the $g_B > 0.5$ region, the blue line is higher than the red line. Near $g_B = 0.5$, the two lines cross, which means that the branching ratios of the two v_S parameters are equal for a given value of g_B . g_B is the coupling constant for the new physical interactions, and for two different values of v_S , $\text{Br}(\mu \rightarrow 3e)$ both show a monotonically decreasing trend with increasing g_B .

Defining the parameters $\tan\beta = 25$, $g_{YB} = 0.1$, $g_B = 0.3$, $v_S = 4$ TeV, $M_2 = 1.2$ TeV, $T_\nu = 1$ TeV, $T_{e12} = 1 \times 10^{-4}$ TeV, $M_L^2 = 0.16$ TeV², $M_E^2 = 1.5$ TeV². Fig.8(d) shows the variation trend of $\text{Br}(\mu \rightarrow 3e)$ with λ under the values of two different parameter $\tan\beta$, where the blue line represents $\tan\beta = 25$ and the red line represents $\tan\beta = 20$. λ is the constant of the $\lambda\hat{S}\hat{H}_u\hat{H}_d$ term in the superpotential and appears in the mass squared matrix of neutralino at tree level. Both lines show a tendency for $\text{Br}(\mu \rightarrow 3e)$ to increase slightly and then gradually decrease as λ increases, with $\text{Br}(\mu \rightarrow 3e)$ reaching a maximum near the value of $\lambda=0.15$. The height of the peak varies with $\tan\beta$, but the overall shape is similar. The $\text{Br}(\mu \rightarrow 3e)$ value at $\tan\beta=20$ is always higher than the value at $\tan\beta=25$.

2. $\tau \rightarrow 3\mu$

The experiment upper bound of the LFV process $\text{Br}(\tau \rightarrow 3\mu)$ is 2.1×10^{-8} , which is four orders of magnitude larger than that of $\mu \rightarrow 3e$. Here it is assumed that $g_{YB} = 0.1$, $g_B = 0.3$, $\lambda = 0.4$, $v_S = 4$ TeV, $M_2 = 1.2$ TeV, $M_E^2 = 1.5$ TeV² to study $\tau \rightarrow 3\mu$.

In order to explore the influence of M_L^2 , M_{L23}^2 on $\tau \rightarrow 3\mu$ in Fig.9(a), we set $T_\nu = 1$ TeV, $\tan\beta = 25$ and perform random scans in the following ranges:

$$\begin{aligned} 0.02 \leq g_{YB} \leq 0.3, \quad 2 \times 10^5 \text{ GeV}^2 \leq M_L^2 \leq 2 \times 10^6 \text{ GeV}^2, \\ -2500 \text{ GeV} \leq T_\nu \leq 2500 \text{ GeV}, \quad 0 \text{ GeV}^2 \leq M_{L23}^2 \leq 1 \times 10^5 \text{ GeV}^2. \end{aligned} \quad (46)$$

As can be seen from Fig.9(a), the variation of $\text{Br}(\tau \rightarrow 3\mu)$ shows a significant dependence. When M_{L23}^2 is small (in the region of vertical coordinate $M_{L23}^2 < 40000$ GeV²), both the changes of M_L^2 and M_{L23}^2 have a weaker effect on the branching ratios, resulting in insensitive changes in branching ratios. This is due to the small contribution of the non-diagonal element M_{L23}^2 to the flavor mixing, while the mass suppression effect of M_L^2 has suppressed the branching ratios to a low level. At larger M_{L23}^2 (in the region of vertical coordinates

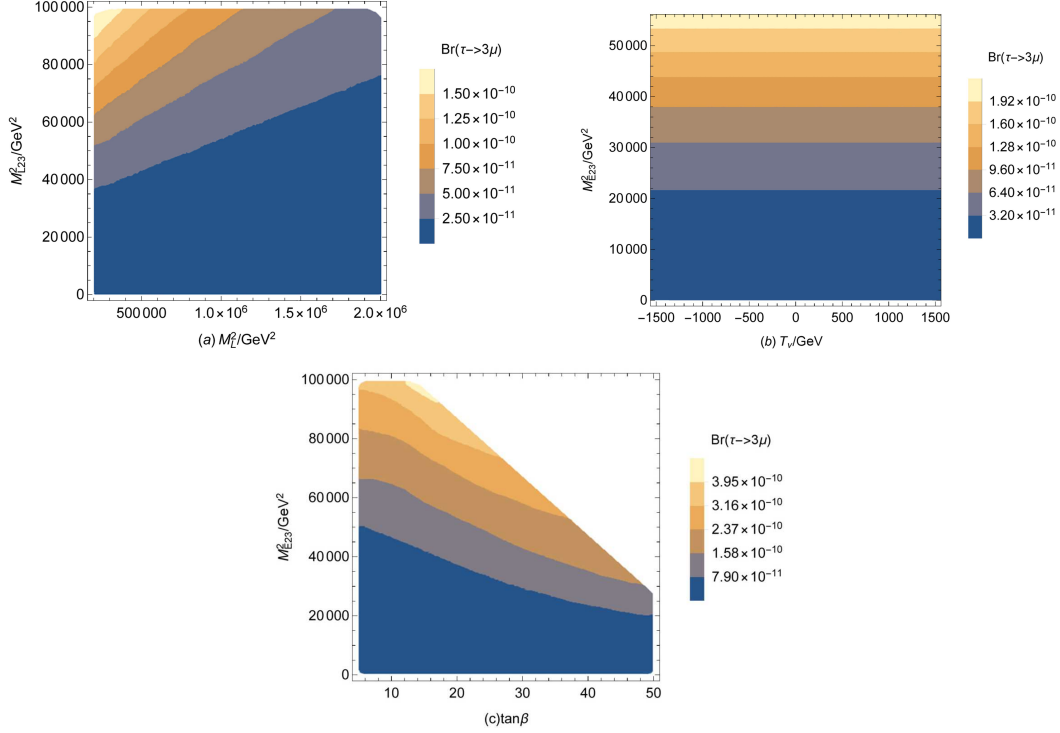


FIG. 9: (a) shows the relationship of M_L^2 and M_{E23}^2 on $\text{Br}(\tau \rightarrow 3\mu)$. The horizontal coordinate indicates the range $2 \times 10^5 \text{ GeV}^2 \leq M_L^2 \leq 2 \times 10^6 \text{ GeV}^2$ and the vertical coordinate indicates the range $0 \text{ GeV}^2 \leq M_{E23}^2 \leq 1 \times 10^5 \text{ GeV}^2$. (b) shows the relationship of T_ν and M_{E23}^2 on $\text{Br}(\tau \rightarrow 3\mu)$. The horizontal coordinate indicates the range $-1500 \text{ GeV} \leq T_\nu \leq 1500 \text{ GeV}$ and the vertical coordinate indicates the range $0 \text{ GeV}^2 \leq M_{E23}^2 \leq 55000 \text{ GeV}^2$. (c) shows the relationship of $\tan\beta$ and M_{E23}^2 on $\text{Br}(\tau \rightarrow 3\mu)$. The horizontal coordinate indicates the range $5 \leq \tan\beta \leq 50$ and the vertical coordinate indicates the range $0 \text{ GeV}^2 \leq M_{E23}^2 \leq 1 \times 10^5 \text{ GeV}^2$. The right icons represent the colors corresponding to the $\text{Br}(\tau \rightarrow 3\mu)$ values.

$M_{E23}^2 > 40000 \text{ GeV}^2$), the dependence of branching ratios on both becomes more pronounced: branching ratios decrease rapidly with increasing M_L^2 , reflecting the dominant effect of mass suppression effects; meanwhile, M_{E23}^2 increase also significantly increases branching ratios, reflecting the contribution of non-diagonal element to enhance flavor mixing. Near the contour line (color boundary), the change in branching ratio presents as a diagonal line, suggesting that an increase in M_{E23}^2 partially compensates for the mass suppression effect of M_L^2 . This suggests that as the non-diagonal element get larger and the diagonal element get smaller, the branching ratio of the $(\tau \rightarrow 3\mu)$ process is closer to the experimental upper

limit.

In Fig.9(b), we set $M_L^2 = 1.6 \times 10^5 \text{ GeV}^2$, $\tan \beta = 25$ to study the effect the two parameters T_ν and M_{E23}^2 together on $\text{Br}(\tau \rightarrow 3\mu)$. The ranges of scattering points are as follows:

$$\begin{aligned} -2500 \text{ GeV} \leq T_\nu \leq 2500 \text{ GeV}, \quad 2 \times 10^5 \text{ GeV}^2 \leq M_L^2 \leq 2 \times 10^6 \text{ GeV}^2, \\ -500 \text{ GeV} \leq T_{e23} \leq 500 \text{ GeV}, \quad 0 \text{ GeV}^2 \leq M_{E23}^2 \leq 1 \times 10^5 \text{ GeV}^2. \end{aligned} \quad (47)$$

It can be seen from Fig.9(b) that $\text{Br}(\tau \rightarrow 3\mu)$ hardly changes with the horizontal coordinate T_ν , but increases completely with the vertical coordinate M_{E23}^2 . T_ν is the parameter related to the non-diagonal element of the sneutrino mass squared matrix, and it follows that in this parameter space $\text{Br}(\tau \rightarrow 3\mu)$ dependence on T_ν is negligible, and the influence of M_{E23}^2 on $\text{Br}(\tau \rightarrow 3\mu)$ predominates.

Let us assume that $M_L^2 = 1.6 \times 10^5 \text{ GeV}^2$, $T_\nu = 1 \text{ TeV}$, we focus on the effect of $\tan \beta$ and M_{E23}^2 on $\text{Br}(\tau \rightarrow 3\mu)$ in Fig.9(c). We randomly scan the parameters as follows:

$$\begin{aligned} 5 \leq \tan \beta \leq 50, \quad 2 \times 10^5 \text{ GeV}^2 \leq M_L^2 \leq 2 \times 10^6 \text{ GeV}^2, \\ -2500 \text{ GeV} \leq T_\nu \leq 2500 \text{ GeV}, \quad 0 \text{ GeV}^2 \leq M_{E23}^2 \leq 1 \times 10^5 \text{ GeV}^2. \end{aligned} \quad (48)$$

Fig.9(c) presents a trapezoidal distribution as a whole, and M_{E23}^2 is a non-diagonal element of slepton mass matrix. The increase of M_{E23}^2 will significantly enhance slepton flavor mixing effect, which brings the same impact as Fig.9(b). Increasing M_{E23}^2 significantly increases $\text{Br}(\tau \rightarrow 3\mu)$, and increasing $\tan \beta$ also increases $\text{Br}(\tau \rightarrow 3\mu)$, but its effect is limited in scope. The white area in the upper right corner of Fig.9(c) may be due to the limitation of the masses of the Higgs particle and other particles.

3. $\tau \rightarrow 3e$

In the same way, we analyze the LFV process $\tau \rightarrow 3e$, whose experimental upper bound is $\text{Br}(\tau \rightarrow 3e) < 2.7 \times 10^{-8}$. In order to get numerical results for $\tau \rightarrow 3e$, we use $\tan \beta = 25$, $g_B = 0.3$, $g_{YB} = 0.1$, $\lambda = 0.4$, $v_S = 4 \text{ TeV}$, $M_2 = 1.2 \text{ TeV}$, $M_L^2 = 1.6 \times 10^5 \text{ GeV}^2$ and carry out two random scattering points to obtain the influence of M_E^2 , M_{E13}^2 , T_ν , M_{L13}^2 on $\text{Br}(\tau \rightarrow 3e) < 2.7 \times 10^{-8}$ in Fig.10 and Fig.11.

The parameters are randomly scanned for the first time. The ranges of parameters are shown in Table IV, and the branching ratio of $\tau \rightarrow 3e$ process is expressed as: \blacklozenge ($0 <$

TABLE IV: Scanning parameters for Fig.10

Parameters	Min	Max
M_L^2/GeV^2	2×10^5	2×10^6
M_{L13}^2/GeV^2	0	10^5
T_ν/GeV	-2500	2500
T_{e13}/GeV	-500	500
$\tan \beta$	5	50

$Br(\tau \rightarrow \mu\gamma) < 1 \times 10^{-11}$), \blacktriangle ($1 \times 10^{-11} \leq Br(\tau \rightarrow \mu\gamma) < 8 \times 10^{-11}$), \bullet ($8 \times 10^{-11} \leq Br(\tau \rightarrow \mu\gamma) < 2.7 \times 10^{-8}$).

Fig.10 illustrates the distributional properties of the branching ratio of $\tau \rightarrow 3e$ in the (T_ν, M_{L13}^2) parameter space. The analysis indicates that when M_{L13}^2 is held constant, $Br(\tau \rightarrow 3e)$ significantly increases with the rise of T_ν , demonstrating that positive T_ν has a pronounced effect on enhancing flavor violation effects. When T_ν is fixed, $Br(\tau \rightarrow 3e)$ markedly grows with the increase of M_{L13}^2 , indicating that the non-diagonal mass term M_{L13}^2 is one of the dominant factors in flavor violation effects.

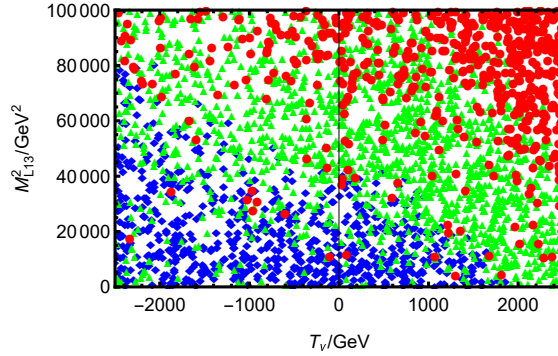


FIG. 10: Under the constraint of $Br(\tau \rightarrow 3e)$ process, a reasonable parameter space is selected for random scattering, and the marking of the scattering points represents: \blacklozenge ($0 < Br(\tau \rightarrow 3e) < 1 \times 10^{-11}$), \blacktriangle ($1 \times 10^{-11} \leq Br(\tau \rightarrow 3e) < 8 \times 10^{-11}$), \bullet ($8 \times 10^{-11} \leq Br(\tau \rightarrow 3e) < 2.7 \times 10^{-8}$).

Then we continue to randomly scatter points, and the parameter ranges are shown in Table V. \blacklozenge , \blacktriangle and \bullet indicate the range $0 < Br(\tau \rightarrow 3e) < 1.3 \times 10^{-11}$, $1.3 \times 10^{-11} \leq Br(\tau \rightarrow 3e) < 8 \times 10^{-11}$, $8 \times 10^{-11} \leq Br(\tau \rightarrow 3e) < 2.7 \times 10^{-8}$.

The distribution of $Br(\tau \rightarrow 3e)$ on the (M_E^2, M_{E13}^2) plane shows an asymmetric "U"

TABLE V: Scanning parameters for Fig.11

Parameters	Min	Max
M_L^2/GeV^2	2×10^5	2×10^6
M_E^2/GeV^2	2×10^5	2×10^6
M_ν^2/GeV^2	1×10^5	2×10^6
M_{E13}^2/GeV^2	0	10^5
T_e/GeV	-2500	2500
T_ν/GeV	-2500	2500

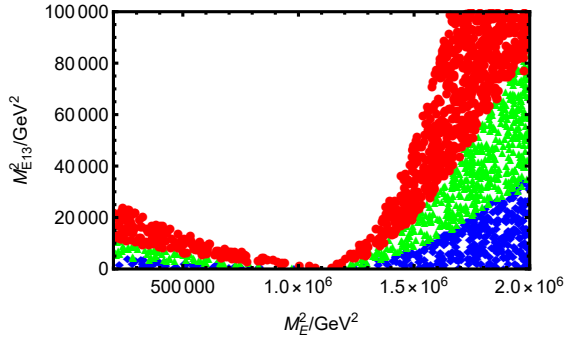


FIG. 11: Under the constraint of $\text{Br}(\tau \rightarrow 3e)$ process, a reasonable parameter space is selected for random scattering, and the marking of the scattering points represents: \blacklozenge ($0 < \text{Br}(\tau \rightarrow 3e) < 1.3 \times 10^{-11}$), \blacktriangle ($1.3 \times 10^{-11} \leq \text{Br}(\tau \rightarrow 3e) < 8 \times 10^{-11}$), \bullet ($8 \times 10^{-11} \leq \text{Br}(\tau \rightarrow 3e) < 2.7 \times 10^{-8}$).

shape with some blank areas in Fig.11. The asymmetry of the "U" shaped distribution in Fig.11 is attributed to the predominance of the diagonal term M_E^2 : when M_E^2 is small, the slepton mass is relatively light, and the influence of the non-diagonal term on the flavor violation effect is more pronounced, making the red region more likely to appear at low M_E^2 with a large M_{E13}^2 . Conversely, when M_E^2 is larger, the diagonal term dominates the slepton mass eigenvalues, and the contribution of the non-diagonal term is relatively suppressed, necessitating a larger M_{E13}^2 for the red region to emerge. It is evident that the action of M_E^2 on $\text{Br}(\tau \rightarrow 3e)$ changes differently on both sides of $M_E^2 \approx 1.1 \times 10^6 \text{ GeV}^2$. For smaller values of M_E^2 ($2 \times 10^5 \text{ GeV}^2 \leq M_E^2 < 1.1 \times 10^6 \text{ GeV}^2$), the mass of slepton is lighter, which leads to stronger flavor violation effect. As M_E^2 increases, the interactions among supersymmetric particles, such as Chargino (χ^\pm) with sneutrino ($\tilde{\nu}$) and neutralino (χ^0) with slepton (\tilde{L}), may become more significant, resulting in the branching ratio to

enhance with M_E^2 . This trend is contrary to the usual expectation, likely because the increase arise from amplified coupling strengths between these particles, intensifying flavor violation effect. In contrast, at larger M_E^2 ($1.1 \times 10^6 \text{ GeV}^2 \leq M_E^2 < 2 \times 10^6 \text{ GeV}^2$), slepton mass grows sufficiently heavy to suppress flavor violation, causing $\text{Br}(\tau \rightarrow 3e)$ to decrease with further increases in M_E^2 , aligning with standard predictions. The peak observed near $M_E^2 \approx 1.1 \times 10^6 \text{ GeV}^2$ corresponds to a maximal branching ratio. Here, slepton mass is elevated but not yet heavy enough to fully suppress flavor violation. At this critical point, interactions between $\chi^0 \tilde{\nu}$ and $\chi^0 \tilde{L}$ reach their strongest effective coupling, optimizing flavor violation contributions to $\tau \rightarrow 3e$. M_{E13}^2 is the non-diagonal term in the slepton mass matrix and governs the mixing between different generations of slepton. Larger M_{E13}^2 enhances this mixing, typically amplifying flavor violation effects and thereby increasing $\text{Br}(\tau \rightarrow 3e)$. In conclusion, when the vertical axis is a constant value, considering the effect of the horizontal axis on $\text{Br}(\tau \rightarrow 3e)$ that the leftward rise in the branching ratio is likely driven by $\chi^0 \tilde{\nu}$ and $\chi^0 \tilde{L}$ interactions, while the subsequent decline at higher M_E^2 reflects the weakening of $\chi^0 \tilde{L}$ couplings due to heavier slepton. The emergence of white region in Fig.11 may be attributed to several factors: the particles masses may exceed the detectable ranges of the LHC; the flavor violation effect may be too significant, surpassing the upper limits of experimental measurements.

C. $\mu \rightarrow e + q\bar{q}$

In this subsection, we discuss numerical results for $\mu \rightarrow e + q\bar{q}$ and consider constraints from the LFV processes $l_j \rightarrow l_i \gamma$ and $l_j \rightarrow 3l_i$. In this work, we use the parameters $T_\nu = 1 \text{ TeV}$, $T_e = 1 \text{ TeV}$, $v_S = 4 \text{ TeV}$, $M_L^2 = 1.6 \times 10^5 \text{ GeV}^2$.

In Fig.12, we set $\tan \beta = 25$, $\lambda = 0.4$, $g_B = 0.3$, $g_{YB} = 0.1$, $M_2 = 1.2 \text{ TeV}$, $M_E^2 = 1.5 \text{ TeV}^2$ and scan some parameters in Table VI. Fig.12(a) demonstrates a strong correlation among $\text{CR}(\mu \rightarrow e:\text{Ti})$, $\text{CR}(\mu \rightarrow e:\text{Pb})$ and $\text{CR}(\mu \rightarrow e:\text{Au})$. The conversion rates of the three are similar by orders of magnitude and have the same growth trend. Therefore, in order to simplify the analysis, it is possible to study only the behavior of $\text{CR}(\mu \rightarrow e:\text{Au})$ without affecting the understanding of the overall physical mechanism. The values of $\text{CR}(\mu \rightarrow e:\text{Au})$ are calculated by satisfying the two experimental constraints $\text{Br}(\mu \rightarrow e\gamma)$ and $\text{Br}(\mu \rightarrow eee)$. Fig.12(b) and Fig.12(c) remains stable under these constraints, their values are not

TABLE VI: Scanning parameters for Fig.12 and Fig.14

Parameters	Min	Max
M_L^2/GeV^2	2×10^5	2×10^6
M_E^2/GeV^2	2×10^5	2×10^6
M_ν^2/GeV^2	1×10^5	2×10^6
M_{E12}^2/GeV^2	0	100
M_2/GeV	900	3000
v_S/GeV	2000	7000
T_{e12}/GeV	0	10
$\tan \beta$	5	50
g_B	0.3	0.6
g_{YB}	0.01	0.2
λ	0.1	0.4

very closely related to $\text{Br}(\mu \rightarrow e\gamma)$ and $\text{Br}(\mu \rightarrow eee)$. This result may reflect the relative independence of different decay processes in a particular parameter space. Based on the above analysis, in order to save space, we only use $\text{CR}(\mu \rightarrow e:\text{Au})$ for the subsequent discussion when $\text{CR}(\mu \rightarrow e:\text{Ti}) < 4.3 \times 10^{-12}$, $\text{CR}(\mu \rightarrow e:\text{Pb}) < 4.6 \times 10^{-11}$ are satisfied, without affecting the universality of the conclusions.

With the parameters $\lambda = 0.4$, $g_B = 0.3$, $g_{YB} = 0.1$, $T_{e12} = 0.1 \text{ GeV}$, $M_E^2 = 1.5 \text{ TeV}^2$, Fig.13(a) shows $\text{CR}(\mu \rightarrow e:\text{Au})$ as a function of $\tan \beta$. It can be seen that $\text{CR}(\mu \rightarrow e:\text{Au})$ decreases as $\tan \beta$ increases. In addition, $M_2 = 2000 \text{ GeV}$ makes $\text{CR}(\mu \rightarrow e:\text{Au})$ significantly higher than the case of $M_2 = 500 \text{ GeV}$. Supposing $\tan \beta = 25$, $g_B = 0.3$, $T_{e12} = 0.1 \text{ GeV}$, $M_2 = 1.2 \text{ TeV}$, $M_E^2 = 1.5 \text{ TeV}^2$, Fig.13(b) examines the trend of $\text{CR}(\mu \rightarrow e:\text{Au})$ as g_{YB} varies, considering two different values of λ : $\lambda = 0.4$ (blue line) and $\lambda = 0.15$ (red line). As can be seen from Fig.13(b), $\text{CR}(\mu \rightarrow e:\text{Au})$ rises monotonically with increasing g_{YB} and smaller λ corresponds to larger conversion rates. Setting $\lambda = 0.4$, $g_B = 0.3$, $g_{YB} = 0.1$, $M_2 = 1.2 \text{ TeV}$, $M_E^2 = 1.5 \text{ TeV}^2$, we plot $\text{CR}(\mu \rightarrow e:\text{Au})$ versus $\tan \beta$ in Fig.13(c), the red line corresponds to $T_{e12} = 0.1 \text{ GeV}$ and the blue line corresponds to $T_{e12} = 0.2 \text{ GeV}$. We can clearly see that the two lines decrease with the increasing $\tan \beta$, and the conversion rate of $T_{e12} = 0.2 \text{ GeV}$ (blue line) is always higher than

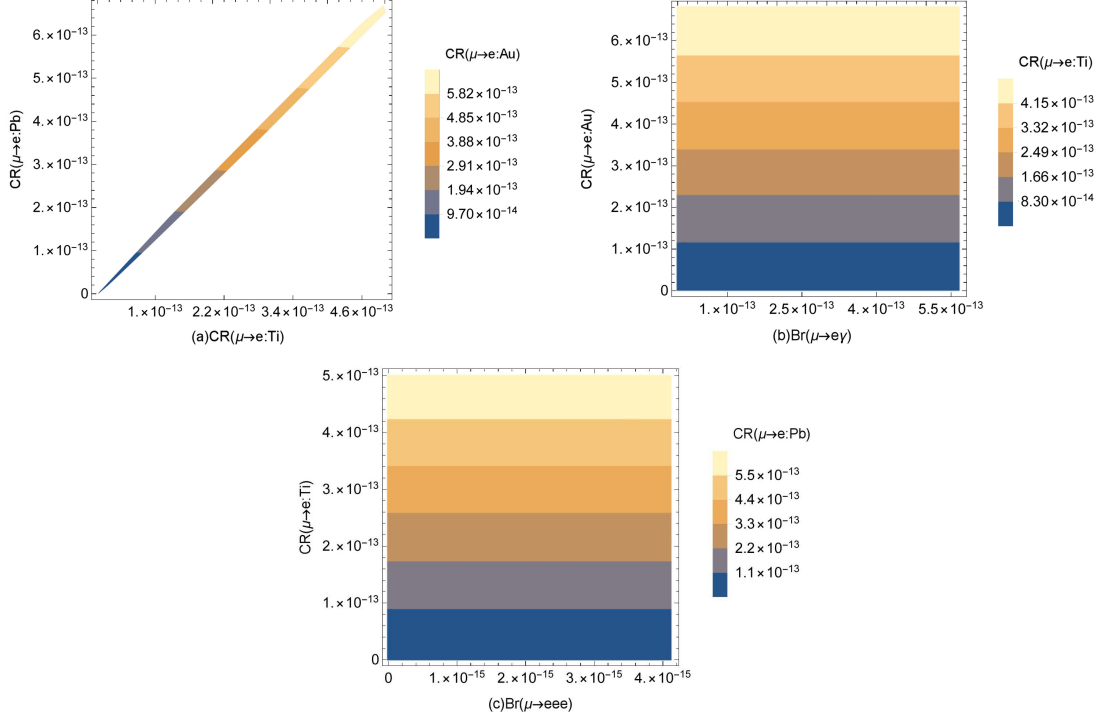


FIG. 12: (a) shows the relationship of $CR(\mu \rightarrow e:Ti)$ and $CR(\mu \rightarrow e:Pb)$ on $CR(\mu \rightarrow e:Au)$. (b) shows the relationship of $Br(\mu \rightarrow e\gamma)$ and $CR(\mu \rightarrow e:Au)$ on $CR(\mu \rightarrow e:Ti)$. (c) shows the relationship of $Br(\mu \rightarrow eee)$ and $CR(\mu \rightarrow e:Ti)$ on $CR(\mu \rightarrow e:Pb)$.

$T_{e12} = 0.1$ GeV (red line). In conclusion, Fig.13(a) and Fig.13(c) show that an increase in $\tan\beta$ leads to a decrease in $CR(\mu \rightarrow e:Au)$. Fig.13(b) shows that g_{YB} , as an important additional parameter, can enhance the LFV process, resulting in a significant increase in conversion rate. In addition, different values of the parameters M_2 , λ and T_{e12} also affect the magnitude of $CR(\mu \rightarrow e:Au)$, suggesting that these parameters play a key role in LFV.

Next, we randomly scan the parameters. Based on $\tan\beta = 25$, $\lambda = 0.4$, $g_{YB} = 0.1$, $M_2 = 1.2$ TeV, Fig.14 is obtained from the parameters shown in Table VI. We use \blacklozenge ($0 < CR(\mu \rightarrow e:Au) < 3 \times 10^{-14}$), \blacktriangle ($3 \times 10^{-14} \leq CR(\mu \rightarrow e:Au) < 2.8 \times 10^{-13}$), \bullet ($2.8 \times 10^{-13} \leq CR(\mu \rightarrow e:Au) < 7 \times 10^{-13}$) to represent the results in different parameter spaces for the process of $\mu \rightarrow e + q\bar{q}$. The relationship between M_E^2 and M_{E12}^2 is shown in Fig.14(a). It is evident from the distribution of data points that $CR(\mu \rightarrow e:Au)$ rises significantly with the increase of M_{E12}^2 , while the dependence on M_E^2 is relatively weak. Specifically, \blacklozenge are mainly in $0 \text{ GeV}^2 < M_{E12}^2 < 20 \text{ GeV}^2$, \blacktriangle are mainly in $20 \text{ GeV}^2 < M_{E12}^2 < 60 \text{ GeV}^2$ and \bullet are mainly in $60 \text{ GeV}^2 < M_{E12}^2 < 100 \text{ GeV}^2$. This trend is consistent with the expectation from

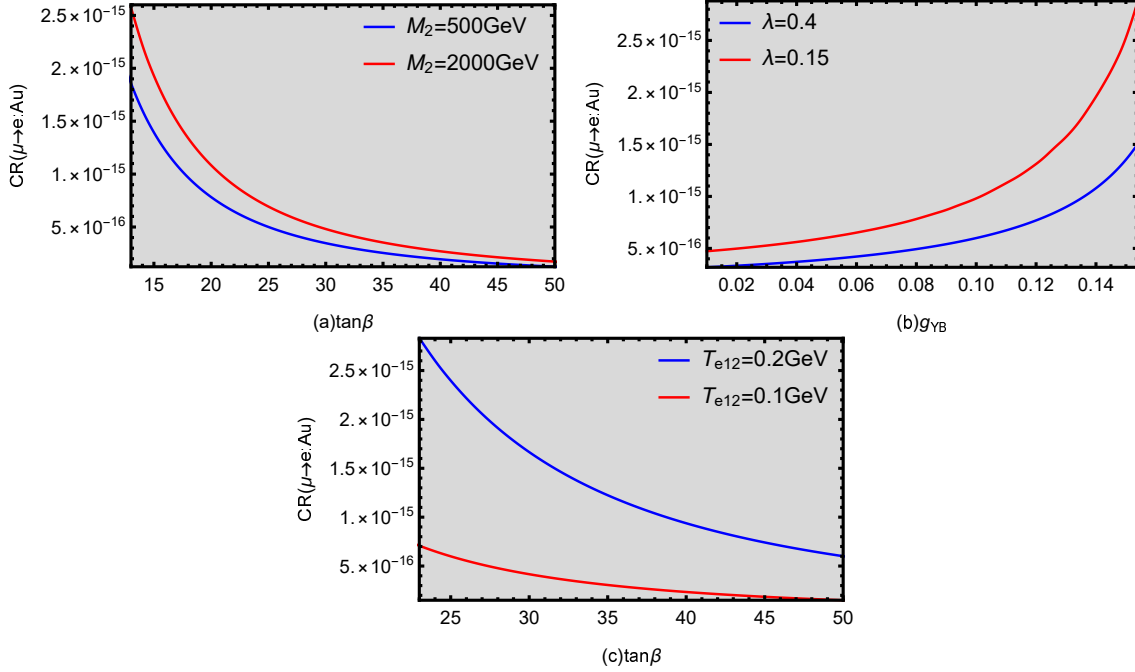


FIG. 13: $CR(\mu \rightarrow e: Au)$ schematic diagrams affected by different parameters, the gray area satisfies the experimental upper limit. Fig.13(a) shows the relationship between $\tan\beta$ and $CR(\mu \rightarrow e: Au)$ with the red line representing $M_2 = 2000 \text{ GeV}$ and the blue line representing $M_2 = 500 \text{ GeV}$. Fig.13(b) shows the relationship between g_{YB} and $CR(\mu \rightarrow e: Au)$ with the red line representing $\lambda = 0.15$ and the blue line representing $\lambda = 0.4$. Fig.8(c) shows the relationship between $\tan\beta$ and $CR(\mu \rightarrow e: Au)$ with the red line representing $T_{e12} = 0.1 \text{ GeV}$ and the blue line representing $T_{e12} = 0.2 \text{ GeV}$.

LFV theory that the non-diagonal term M_{E12}^2 directly controls the flavor mixing strength of the slepton mass matrix, thereby enhancing the amplitude of the jump of the LFV process leading to a larger $CR(\mu \rightarrow e: Au)$. In contrast, M_E^2 mainly affects the slepton mass scale, and its effect on $CR(\mu \rightarrow e: Au)$ is small within the given parameter ranges, so the data points do not show a significant trend in the M_E^2 direction. Fig.14(b) shows the distribution of $CR(\mu \rightarrow e: Au)$ for different M_{E12}^2 and g_B values. One can see that $CR(\mu \rightarrow e: Au)$ primarily rises with M_{E12}^2 , bringing about the same effect as in Fig.14(a). The effect of g_B on the conversion rate is also present to some extent, although its effect is not as significant as that of M_{E12}^2 . In the larger g_B region, the density of data points is higher, while in the smaller g_B region, the data points are more sparse.

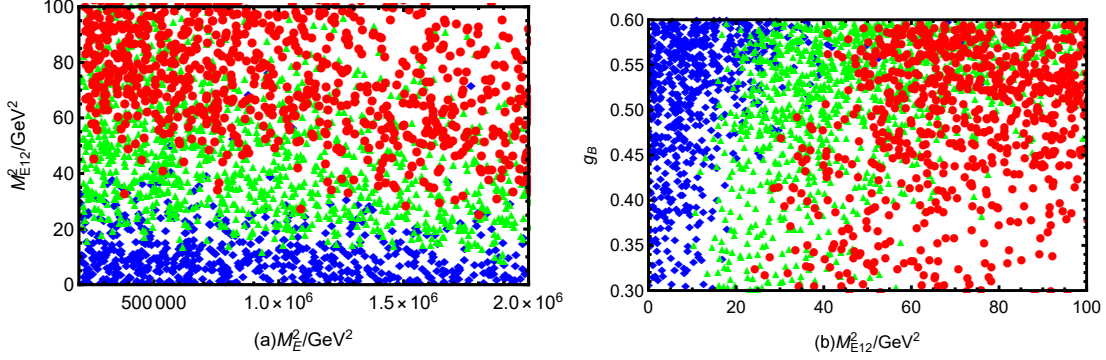


FIG. 14: Under the constraint of $\text{CR}(\mu \rightarrow e:\text{Au})$ process, a reasonable parameter space is selected for random scattering, and the marking of the scattering points represents: \blacklozenge ($0 < \text{CR}(\mu \rightarrow e:\text{Au}) < 3 \times 10^{-14}$), \blacktriangle ($3 \times 10^{-14} \leq \text{CR}(\mu \rightarrow e:\text{Au}) < 2.8 \times 10^{-13}$), \bullet ($2.8 \times 10^{-13} \leq \text{CR}(\mu \rightarrow e:\text{Au}) < 7 \times 10^{-13}$).

V. DISCUSSION AND CONCLUSION

In the SM, the LFV decays $l_j \rightarrow l_i \gamma$ and $l_j \rightarrow 3l_i$ have extremely low predicted branching ratios. For example, the branching ratio $\text{Br}(\mu \rightarrow e \gamma) \sim 10^{-55}$ is much lower than the current experimental upper limit of 10^{-13} , rendering these decays virtually unobservable in the SM. Similarly, the $\mu \rightarrow e + q \bar{q}$ conversion rate is predicted to be negligibly small. Therefore, if signals of these LFV processes are experimentally detected, they would necessarily indicate NP beyond the SM. Within the framework of the N-B-LSSM, we analyze the contributions of the newly introduced particles and couplings to LFV processes by calculating the corresponding Feynman diagrams and performing an extensive parameter space scan. Compared with the MSSM, the N-B-LSSM introduces additional superfields, including right-handed neutrinos and three Higgs superfields, which not only help resolve certain issues in the MSSM but also provide extra sources for LFV, thereby significantly enhancing the LFV signals.

The experimental limits on the branching ratios for $\mu \rightarrow e \gamma$ and $\mu \rightarrow 3e$, as well as on the conversion rate for $\mu \rightarrow e + q \bar{q}$ are extremely stringent, which strongly constrains the theoretical parameter space. In contrast, the experimental upper limits for $\tau \rightarrow e \gamma$, $\tau \rightarrow \mu \gamma$, $\tau \rightarrow 3e$ and $\tau \rightarrow 3\mu$ are around 10^{-8} orders of magnitude, imposing relatively looser constraints. Our results indicate that parameters such as $\tan \beta$, g_B , g_{YB} , v_S , λ , T_e , T_ν , T_{eij} , $T_{\nu ij}$, M_2 , M_L^2 , M_E^2 , M_{Lij}^2 , M_{Eij}^2 and $M_{\nu ij}^2$ ($i, j = 1, 2, 3$, $i \neq j$) have varying degrees of influence on LFV processes, with M_{Lij}^2 , M_{Eij}^2 , $M_{\nu ij}^2$, T_{eij} , $T_{\nu ij}$, g_B , g_{YB} and $\tan \beta$ being particularly sensitive. In conclusion, through the analysis of lepton flavour mixing

parameters, we find that the non-diagonal elements which correspond to the generations of the initial lepton and final lepton are main sensitive parameters and LFV sources. Most of the parameters are able to break the experimental upper limit, providing new ideas for the search of NP.

Acknowledgments

This work is supported by National Natural Science Foundation of China (NNSFC) (No.12075074), Natural Science Foundation of Hebei Province (A2023201040, A2022201022, A2022201017, A2023201041), Natural Science Foundation of Hebei Education Department (QN2022173), Post-graduate's Innovation Fund Project of Hebei University (HBU2024SS042), the Project of the China Scholarship Council (CSC) No. 202408130113.

Appendix A: Mass matrix and coupling in N-B-LSSM

The mass matrix for neutralino $(\lambda_{\tilde{B}}, \tilde{W}^0, \tilde{H}_d^0, \tilde{H}_u^0, \tilde{B}', \tilde{\chi}_1, \tilde{\chi}_2, S)$ reads:

$$m_{\chi^0} = \begin{pmatrix} M_1 & 0 & -\frac{1}{2}g_1v_d & \frac{1}{2}g_1v_u & M_{BB'} & 0 & 0 & 0 \\ 0 & M_2 & \frac{1}{2}g_2v_d & -\frac{1}{2}g_2v_u & 0 & 0 & 0 & 0 \\ -\frac{1}{2}g_1v_d & \frac{1}{2}g_2v_d & 0 & -\frac{1}{\sqrt{2}}\lambda v_S & -\frac{1}{2}g_{YB}v_d & 0 & 0 & -\frac{1}{\sqrt{2}}\lambda v_u \\ \frac{1}{2}g_1v_u & -\frac{1}{2}g_2v_u & -\frac{1}{\sqrt{2}}\lambda v_S & 0 & \frac{1}{2}g_{YB}v_u & 0 & 0 & -\frac{1}{\sqrt{2}}\lambda v_d \\ M_{BB'} & 0 & -\frac{1}{2}g_{YB}v_d & \frac{1}{2}g_{YB}v_u & M_{BL} & -g_Bv_\eta & g_Bv_{\tilde{\eta}} & 0 \\ 0 & 0 & 0 & 0 & -g_Bv_\eta & 0 & -\frac{1}{\sqrt{2}}\lambda_2v_S & -\frac{1}{\sqrt{2}}\lambda_2v_{\tilde{\eta}} \\ 0 & 0 & 0 & 0 & g_Bv_{\tilde{\eta}} & -\frac{1}{\sqrt{2}}\lambda_2v_S & 0 & -\frac{1}{\sqrt{2}}\lambda_2v_\eta \\ 0 & 0 & -\frac{1}{\sqrt{2}}\lambda v_u & -\frac{1}{\sqrt{2}}\lambda v_d & 0 & -\frac{1}{\sqrt{2}}\lambda_2v_{\tilde{\eta}} & -\frac{1}{\sqrt{2}}\lambda_2v_\eta & \sqrt{2}\kappa v_S \end{pmatrix}. \quad (\text{A1})$$

This matrix is diagonalized by the rotation matrix N ,

$$N^* m_{\chi^0} N^\dagger = m_{\chi^0}^{dia}. \quad (\text{A2})$$

In the basis $(\tilde{W}^-, \tilde{H}_d^-)$ and $(\tilde{W}^+, \tilde{H}_u^+)$, the definition of the mass matrix for chargino is given by:

$$m_{\tilde{\chi}^\pm} = \begin{pmatrix} M_2 & \frac{1}{\sqrt{2}}g_2v_u \\ \frac{1}{\sqrt{2}}g_2v_d & \frac{1}{\sqrt{2}}\lambda v_S \end{pmatrix}. \quad (\text{A3})$$

This matrix is diagonalized by U and V:

$$U^* m_{\tilde{\chi}^-} V^\dagger = m_{\tilde{\chi}^-}^{dia}. \quad (\text{A4})$$

The mass matrix for slepton in the basis $(\tilde{e}_L, \tilde{e}_R), (\tilde{e}_L^*, \tilde{e}_R^*)$ is:

$$m_{\tilde{e}}^2 = \begin{pmatrix} m_{\tilde{e}_L \tilde{e}_L^*} & \frac{1}{\sqrt{2}} v_d T_e^\dagger - \frac{1}{2} \lambda v_S v_u Y_e^\dagger \\ \frac{1}{\sqrt{2}} v_d T_e - \frac{1}{2} v_S v_u Y_e \lambda^* & m_{\tilde{e}_R \tilde{e}_R^*} \end{pmatrix}, \quad (\text{A5})$$

$$\begin{aligned} m_{\tilde{e}_L \tilde{e}_L^*} &= \frac{1}{8} \left((g_1^2 + g_{YB}^2 + g_{YB} g_B - g_2^2)(v_d^2 - v_u^2) + 2(g_B^2 + g_{YB} g_B)(v_\eta^2 - v_{\bar{\eta}}^2) \right) \\ &\quad + \frac{1}{2} v_d^2 Y_e^\dagger Y_e + m_{\tilde{L}}^2, \\ m_{\tilde{e}_R \tilde{e}_R^*} &= \frac{1}{8} \left((2g_1^2 + 2g_{YB}^2 + g_{YB} g_B)(v_u^2 - v_d^2) + 2(2g_{YB} g_B + g_B^2)(v_\eta^2 - v_{\bar{\eta}}^2) \right) \\ &\quad + \frac{1}{2} v_d^2 Y_e Y_e^\dagger + m_{\tilde{E}}^2. \end{aligned} \quad (\text{A6})$$

The unitary matrix Z^E is used to rotate slepton mass squared matrix to mass eigenstates:

$$Z^E m_{\tilde{e}}^2 Z^{E,\dagger} = m_{2,\tilde{e}}^{dia}. \quad (\text{A7})$$

The mass squared matrix for CP-even sneutrino (ϕ_l, ϕ_r) reads:

$$m_{\tilde{\nu}R}^2 = \begin{pmatrix} m_{\phi_l \phi_l} & m_{\phi_r \phi_l}^T \\ m_{\phi_l \phi_r} & m_{\phi_r \phi_r} \end{pmatrix}, \quad (\text{A8})$$

$$\begin{aligned} m_{\phi_l \phi_l} &= \frac{1}{8} \left((g_1^2 + g_{YB}^2 + g_2^2 + g_{YB} g_B)(v_d^2 - v_u^2) + 2(g_{YB} g_B + g_B^2)(v_\eta^2 - v_{\bar{\eta}}^2) \right) \\ &\quad + \frac{1}{2} v_u^2 Y_\nu^T Y_\nu^* + m_{\tilde{L}}^2, \end{aligned} \quad (\text{A9})$$

$$m_{\phi_l \phi_r} = -\frac{1}{2} v_d v_S Y_\nu \lambda^* + v_u v_\eta Y_X Y_\nu^* + \frac{1}{\sqrt{2}} v_u T_\nu, \quad (\text{A10})$$

$$\begin{aligned} m_{\phi_r \phi_r} &= \frac{1}{8} \left(g_{YB} g_B (v_u^2 - v_d^2) + 2g_B^2 (v_\eta^2 - v_{\bar{\eta}}^2) \right) - v_S v_{\bar{\eta}} Y_X \lambda_2^* + m_{\tilde{\nu}}^2 + \frac{1}{2} v_u^2 Y_\nu Y_\nu^\dagger \\ &\quad + v_\eta (2v_\eta Y_X Y_X^* + \sqrt{2} T_X). \end{aligned} \quad (\text{A11})$$

To obtain the mass of CP-even sneutrino, we diagonalize the matrix $m_{\tilde{\nu}R}^2$ using the rotation matrix Z^R :

$$Z^R m_{\tilde{\nu}R}^2 Z^{R,\dagger} = m_{2,\tilde{\nu}R}^{dia}. \quad (\text{A12})$$

The mass squared matrix for CP-odd sneutrino (σ_l, σ_r) is also derived here:

$$m_{\tilde{\nu}^I}^2 = \begin{pmatrix} m_{\sigma_l \sigma_l} & m_{\sigma_r \sigma_l}^T \\ m_{\sigma_l \sigma_r} & m_{\sigma_r \sigma_r} \end{pmatrix}, \quad (\text{A13})$$

$$m_{\sigma_l \sigma_l} = \frac{1}{8} \left((g_1^2 + g_{YB}^2 + g_2^2 + g_{YB} g_B)(v_d^2 - v_u^2) + 2(g_B^2 + g_{YB} g_B)(v_\eta^2 - v_{\bar{\eta}}^2) \right) + \frac{1}{2} v_u^2 Y_\nu^T Y_\nu^* + m_{\tilde{L}}^2, \quad (\text{A14})$$

$$m_{\sigma_l \sigma_r} = -\frac{1}{2} v_d v_S Y_\nu \lambda^* - v_u v_\eta Y_X Y_\nu^* + \frac{1}{\sqrt{2}} v_u T_\nu, \quad (\text{A15})$$

$$m_{\sigma_r \sigma_r} = \frac{1}{8} \left(g_{YB} g_B (v_u^2 - v_d^2) + 2g_B^2 (v_\eta^2 - v_{\bar{\eta}}^2) \right) + v_S v_{\bar{\eta}} Y_X \lambda_2^* + m_{\tilde{\nu}}^2 + \frac{1}{2} v_u^2 Y_\nu Y_\nu^\dagger + v_\eta (2v_\eta Y_X Y_X^* - \sqrt{2} T_X). \quad (\text{A16})$$

This matrix is diagonalized by Z^I :

$$Z^I m_{\tilde{\nu}^I}^2 Z^{I,\dagger} = m_{2,\tilde{\nu}^I}^{dia}. \quad (\text{A17})$$

In the basis $(\tilde{u}_L^0, \tilde{u}_R^0)$ and $(\tilde{u}_L^{0,*}, \tilde{u}_R^{0,*})$, the mass squared matrix for up-squark is:

$$m_{\tilde{u}}^2 = \begin{pmatrix} m_{\tilde{u}_L^0 \tilde{u}_L^{0,*}} & \frac{1}{\sqrt{2}} v_u T_u^\dagger - \frac{1}{2} v_d \lambda v_S Y_u^\dagger \\ \frac{1}{\sqrt{2}} v_u T_u - \frac{1}{2} v_d \lambda^* v_S Y_u & m_{\tilde{u}_R^0 \tilde{u}_R^{0,*}} \end{pmatrix}, \quad (\text{A18})$$

$$m_{\tilde{u}_L^0 \tilde{u}_L^{0,*}} = \frac{1}{24} \left((g_1^2 + g_{YB}^2 - 3g_2^2 + g_{YB} g_B)(v_u^2 - v_d^2) + 2(g_B^2 + g_{YB} g_B)(v_\eta^2 - v_{\bar{\eta}}^2) \right) + \frac{1}{2} v_u^2 Y_u^\dagger Y_u + m_{\tilde{Q}}^2, \\ m_{\tilde{u}_R^0 \tilde{u}_R^{0,*}} = \frac{1}{24} \left((4g_1^2 + 4g_{YB}^2 + g_{YB} g_B)(v_d^2 - v_u^2) + 2(4g_{YB} g_B + g_B^2)(v_\eta^2 - v_{\bar{\eta}}^2) \right) + \frac{1}{2} v_u^2 Y_u Y_u^\dagger + m_{\tilde{U}}^2. \quad (\text{A19})$$

This matrix is diagonalized by Z^U :

$$Z^U m_{\tilde{u}}^2 Z^{U,\dagger} = m_{2,\tilde{u}}^{dia}. \quad (\text{A20})$$

In the same way, we obtain the mass squared matrix for down-squark:

$$m_{\tilde{d}}^2 = \begin{pmatrix} m_{\tilde{d}_L^0 \tilde{d}_L^{0,*}} & \frac{1}{\sqrt{2}} v_d T_d^\dagger - \frac{1}{2} v_u \lambda v_S Y_d^\dagger \\ \frac{1}{\sqrt{2}} v_d T_d - \frac{1}{2} v_u \lambda^* v_S Y_d & m_{\tilde{d}_R^0 \tilde{d}_R^{0,*}} \end{pmatrix}, \quad (\text{A21})$$

$$\begin{aligned}
m_{\tilde{d}_L^0 \tilde{d}_L^{0,*}} &= \frac{1}{24} \left((g_1^2 + g_{YB}^2 + 3g_2^2 + g_{YB}g_B)(v_u^2 - v_d^2) + 2(g_B^2 + g_{YB}g_B)(v_\eta^2 - v_\eta^2) \right) \\
&\quad + \frac{1}{2} v_d^2 Y_d^\dagger Y_d + m_{\tilde{Q}}^2, \\
m_{\tilde{d}_R^0 \tilde{d}_R^{0,*}} &= \frac{1}{24} \left((g_{YB}g_B - 2g_1^2 - 2g_{YB}^2)(v_d^2 - v_u^2) + 2(g_B^2 - 2g_{YB}g_B)(v_\eta^2 - v_\eta^2) \right) \\
&\quad + \frac{1}{2} v_d^2 Y_d Y_d^\dagger + m_{\tilde{D}}^2.
\end{aligned} \tag{A22}$$

This matrix is diagonalized by Z^D :

$$Z^D m_{\tilde{d}}^2 Z^{D,\dagger} = m_{2,d}^{dia}. \tag{A23}$$

To save space in the text, other mass matrixes can be found in Ref. [15].

We clarify certain couplings that are required for subsequent applications within the framework of this model. In the below equations, $P_L = \frac{1}{2}(1 - \gamma_5)$, $P_R = \frac{1}{2}(1 + \gamma_5)$.

1. The vertexes of $\bar{l}_i - \chi_j^- - \tilde{\nu}_k^R (\tilde{\nu}_k^I)$

$$\begin{aligned}
\mathcal{L}_{\bar{l}_i \chi_j^- \tilde{\nu}_k^R} &= \frac{1}{\sqrt{2}} \bar{l}_i \left\{ U_{j2}^* Z_{ki}^{R*} Y_l^i P_L - g_2 V_{j1} Z_{ki}^{R*} P_R \right\} \chi_j^- \tilde{\nu}_k^R, \\
\mathcal{L}_{\bar{l}_i \chi_j^- \tilde{\nu}_k^I} &= \frac{i}{\sqrt{2}} \bar{l}_i \left\{ U_{j2}^* Z_{ki}^{I*} Y_l^i P_L - g_2 V_{j1} Z_{ki}^{I*} P_R \right\} \chi_j^- \tilde{\nu}_k^I.
\end{aligned} \tag{A24}$$

2. The vertexes of $\bar{\chi}_i^0 - l_j - \tilde{L}_k$

$$\begin{aligned}
\mathcal{L}_{\bar{\chi}_i^0 l_j \tilde{L}_k} &= \bar{\chi}_i^0 \left\{ \left[\frac{1}{\sqrt{2}} \left(g_1 N_{i1}^* + g_2 N_{i2}^* + (g_{YB} + g_B) N_{i5}^* \right) Z_{kj}^E - N_{i3}^* Y_l^j Z_{k(3+j)}^E \right] P_L \right. \\
&\quad \left. - \left[\frac{1}{\sqrt{2}} \left(2g_1 N_{i1} + (2g_{YB} + g_B) N_{i5} \right) Z_{k(3+j)}^E + Y_l^j Z_{kj}^E N_{i3} \right] P_R \right\} l_j \tilde{L}_k.
\end{aligned} \tag{A25}$$

3. The vertexes of $Z_\mu - \chi_i^\pm - \chi_j^\pm$

$$\begin{aligned}
\mathcal{L}_{Z \chi^\pm \chi^\pm} &= \bar{\chi}_i^\pm \left\{ \frac{1}{2} \left(2g_2 U_{j1}^* \cos \theta_W \cos \theta'_W U_{i1} + U_{j2}^* (-g_1 \cos \theta'_W \sin \theta_W \right. \right. \\
&\quad \left. \left. + g_2 \cos \theta_W \cos \theta'_W + g_{YB} \sin \theta'_W) U_{i2} \right) \gamma_\mu P_L \right. \\
&\quad \left. + \frac{1}{2} \left(2g_2 V_{i1}^* \cos \theta_W \cos \theta'_W V_{j1} + V_{i2}^* (-g_1 \cos \theta'_W \sin \theta_W \right. \right. \\
&\quad \left. \left. + g_2 \cos \theta_W \cos \theta'_W + g_{YB} \sin \theta'_W) V_{j2} \right) \gamma_\mu P_R \right\} \chi_j^\pm Z_\mu.
\end{aligned} \tag{A26}$$

4. The vertex of $Z - \tilde{e}_i - \tilde{e}_j^*$

$$\begin{aligned}
\mathcal{L}_{Z \tilde{e} \tilde{e}^*} &= \frac{1}{2} \tilde{e}_j^* \left[\left(g_2 \cos \theta_W \cos \theta'_W - g_1 \cos \theta'_W \sin \theta_W + (g_{YB} + g_B) \sin \theta'_W \right) \sum_{a=1}^3 Z_{i,a}^{E,*} Z_{j,a}^E \right. \\
&\quad \left. + \left((2g_{YB} + g_B) \sin \theta'_W - 2g_1 \cos \theta'_W \sin \theta_W \right) \sum_{a=1}^3 Z_{i,3+a}^{E,*} Z_{j,3+a}^E \right] (p_i^\mu - p_j^\mu) \tilde{e}_i Z_\mu.
\end{aligned} \tag{A27}$$

5. The quark-related vertices

$$\begin{aligned}\mathcal{L}_{\chi^0 d \tilde{D}} = & -\frac{i}{6} \bar{\chi}_i^0 \left\{ \left[\sqrt{2} \left(g_1 N_{1i} - 3g_2 N_{2i} + (g_{YB} + g_B) N_{5i} \right) Z_{jk}^{\tilde{D}*} + 6N_{3i} Y_d^j Z_{(3+j)k}^{\tilde{D}*} \right] P_L \right. \\ & \left. + \left[6Y_d^j Z_{jk}^{\tilde{D}*} N_{3i}^* + \sqrt{2} Z_{(3+j)k}^{\tilde{D}*} \left(2g_1 N_{1i}^* + (2g_{YB} - g_B) N_{5i}^* \right) \right] P_R \right\} d_j \tilde{D}_k^*, \quad (\text{A28})\end{aligned}$$

$$\begin{aligned}\mathcal{L}_{\chi^0 u \tilde{U}} = & -\frac{i}{6} \bar{\chi}_i^0 \left\{ \left[\sqrt{2} \left(g_1 N_{1i} + 3g_2 N_{2i} + (g_{YB} + g_B) N_{5i} \right) Z_{jk}^{\tilde{U}*} + 6N_{4i} Y_u^j Z_{(3+j)k}^{\tilde{U}*} \right] P_L \right. \\ & \left. - \left[\sqrt{2} Z_{(3+j)k}^{\tilde{U}*} \left((g_B + 4g_{YB}) N_{5i}^* + 4g_1 N_{1i}^* \right) - 6Y_u^j Z_{jk}^{\tilde{U}*} N_{4i}^* \right] P_R \right\} u_j \tilde{U}_k^*, \quad (\text{A29})\end{aligned}$$

$$\mathcal{L}_{\chi^- d \tilde{U}} = \bar{d}_i \left\{ U_{j2}^* \sum_{a=1}^3 Z_{ki}^{\tilde{U}*} Y_d^i P_L + \left[\sum_{a=1}^3 Y_u^i Z_{k(3+i)}^{\tilde{U}*} V_{j2} - g_2 \sum_{a=1}^3 Z_{ki}^{\tilde{U}*} V_{j1} \right] P_R \right\} \chi_i^- \tilde{U}_k^*, \quad (\text{A30})$$

$$\mathcal{L}_{\chi^- u \tilde{D}} = \bar{\chi}_i^- \left\{ \left[U_{i2}^* \sum_{a=1}^3 Y_d^j Z_{k(3+j)}^{\tilde{D}} - g_2 U_{i1}^* \sum_{a=1}^3 Z_{kj}^{\tilde{D}} \right] P_L + \sum_{a=1}^3 Z_{kj}^{\tilde{D}} Y_u^{j*} V_{i2} P_R \right\} u_j \tilde{D}_k^*. \quad (\text{A31})$$

-
- [1] K. Abe et al., *Phys. Rev. Lett.* **107** (2011) 041801.
 - [2] J. Ahn et al., *Phys. Rev. Lett.* **108** (2012) 191802.
 - [3] F. An et al., *Phys. Rev. Lett.* **108** (2012) 171803.
 - [4] E. Ma, A. Natale, O. Popov, *Phys. Lett. B* **746** (2015) 114-116.
 - [5] I. Girardi, S.T. Petcov, A.V. Titov, *Nucl. Phys. B* **894** (2015) 733-768.
 - [6] P. Ghosh, S. Roy, *J. High Energy Phys.* **0904** (2009) 069.
 - [7] P. Ghosh, P. Dey, B. Mukhopadhyaya, S. Roy, *J. High Energy Phys.* **1005** (2010) 087.
 - [8] S. T. Petcov, *Sov. J. Nucl. Phys.* **25** (1977) 340.
 - [9] S. Navas et al., *Phys. Rev. D* **110** (2024) 3, 030001.
 - [10] P. Paradisi, *J. High Energy Phys.*, **10** (2005) 006.
 - [11] J. Gierbach, S. Mertens, U. Nierste and S. Wiesenfeldt, *J. High Energy Phys.* **05** (2010) 026.
 - [12] J. Rosiek, P. H. Chankowski, A. Dedes, S. Jager and P. Tanedo, *Comput. Phys. Commun.* **181** (2010) 2180.
 - [13] U. Ellwanger, C. Hugonie, A.M. Teixeira, *Phys. Rep.* **496** (2010) 1-77.
 - [14] B. Yan, S.M. Zhao, T.F. Feng, *Nucl. Phys. B* **975** (2022) 115671.
 - [15] X.Y. Han, S.M. Zhao, L. Ruan, et al., *Eur. Phys. J. C* **85** (2025) 2, 163.

- [16] H.B. Zhang, T.F. Feng, L.N. Kou, et al., *Int.J.Mod.Phys. A* **28** (2013) 24, 1350117.
- [17] H.B. Zhang, T.F. Feng, S.M. Zhao, et al., *Nucl.Phys. B* **873** (2013) 300-324, Erratum: *Nucl. Phys. B* **879** (2014) 235.
- [18] A. Ilakovac, A. Pilaftsis, L. Popov, *Phys. Rev. D* **87** (2013) 053014.
- [19] J. Hisano, T. Moroi, K. Tobe, et al., *Phys. Rev. D* **53** (1996) 2442.
- [20] P.F. Perez, M.B. Wise, *J. High Energy Phys.* **1108** (2011) 068.
- [21] P.F. Perez, M.B. Wise, *Phys. Rev. D* **82** (2010) 011901.
- [22] T. Guo, S.M. Zhao, X.X. Dong, et al., *Eur. Phys. J. C* **78** (2018) 11, 925.
- [23] M. Carena, J.R. Espinosa, C.E.M. Wagner, et al., *Phys. Lett. B.* **355** (1995) 209.
- [24] M. Carena, S. Gori, N.R. Shah, et al., *J. High Energy Phys.* **1203** (2012) 014.
- [25] G. Belanger, J.D. Silva, H.M. Tran, *Phys. Rev. D* **95** (2017) 115017.
- [26] V. Barger, P.F. Perez, S. Spinner, *Phys. Rev. Lett.* **102** (2009) 181802.
- [27] P.H. Chankowski, S. Pokorski, J. Wagner, *Eur. Phys. J. C* **47** (2006) 187.
- [28] J.L. Yang, T.F. Feng, S.M. Zhao, et al., *Eur. Phys. J. C* **78** (2018) 714.
- [29] J. Bernabeu, E. Nardi, D. Tommasini, *Nucl. Phys. B* **409** (1993) 69-86.
- [30] J.C. Sens, *Phys. Rev.* **113** (1959), 679-687.
- [31] H.C. Chiang, E. Oset, T.S. Kosmas, et al., *Nucl. Phys. A* **559** (1993) 526.
- [32] R. Kitano, M. Koike, Y. Okada, *Phys. Rev. D* **66** (2002) 096002.
- [33] CMS collaboration, *Phys. Lett. B* **716** (2012) 30.
- [34] ATLAS collaboration, *Phys. Lett. B* **716** (2012) 1.
- [35] P. Cox, C.C. Han, and T.T. Yanagida, *Phys. Rev. D* **104** (2021) 075035.
- [36] M.V. Beekveld, W. Beenakker, M. Schutten, et al., *SciPost Phys.* **11** (2021) 3, 049.
- [37] M. Chakraborti, L. Roszkowski and S. Trojanowski, *J. High Energy Phys.* **05** (2021) 252.
- [38] F. Wang, L. Wu, Y. Xiao, et al., *Nucl. Phys. B* **970** (2021) 115486.
- [39] M. Chakraborti, S. Heinemeyer and I. Saha, *Eur. Phys. J. C* **81** (2021) 12, 1114.
- [40] M. Endo, K. Hamaguchi, S. Iwamoto, et al., *J. High Energy Phys.* **07** (2021) 075.
- [41] L. Basso, *Adv. High Energy Phys.* **2015** (2015) 980687.
- [42] ATLAS collaboration, *Phys. Lett. B* **796** (2019) 68.
- [43] G. Cacciapaglia, C. Csáki, G. Marandella, et al., *Phys. Rev. D* **74** (2006) 033011.
- [44] M. Carena, A. Daleo, B. A. Dobrescu, et al., *Phys. Rev. D* **70** (2004) 093009.
- [45] M. Drees, M. Gluck and K. Grassie, *Phys. Lett. B* **157** (1985) 164-168.

- [46] U. Chattopadhyay, D. Das and S. Mukherjee, *J. High Energy Phys.* **06** (2020) 015.
- [47] S.M. Zhao, T.F. Feng, H.B. Zhang, et al., *J. High Energy Phys.* **92** (2015) 115016.
- [48] S.M. Zhao, L.H. Su, X.X. Dong, et al., *J. High Energy Phys.* **03** (2022) 101.
- [49] Muon g-2 collaboration, *Phys. Rev. D* **73** (2006) 072003.
- [50] Muon g-2 collaboration, *Phys. Rev. Lett.* **126** (2021) 141801.